scientific reports

OPEN

Mesoporous Ag@WO$_3$ core–shell, an investigation at different concentrated environment employing laser ablation in liquid

Evan T. Salim[1✉], Jehan A. Saimon[1], Maryam S. Muhsin[1], Makram A. Fakhri[2✉], Mustafa H. Amin[3], Ahmad S. Azzahrani[4✉] & Raed Khalid Ibrahim[5]

In this study, silver-tungsten oxide core–shell nanoparticles (Ag–WO$_3$ NPs) were synthesized by pulsed laser ablation in liquid employing a (1.06 µm) Q-switched Nd:YAG laser, at different Ag colloidal concentration environment (different core concentration). The produced Ag–WO$_3$ core–shell NPs were subjected to characterization using UV–visible spectrophotometry, X-ray diffraction (XRD), transmission electron microscopy (TEM), energy-dispersive spectroscopy, electrical analysis, and photoluminescence PL. The UV–visible spectra exhibited distinct absorption peaks at around 200 and 405 nm, which attributed to the occurrence of surface Plasmon resonance of Ag NPs and WO$_3$ NPs, respectively. The absorbance values of the Ag–WO$_3$ core–shell NPs increased as the core concentrations rose, while the band gap decreased by 2.73–2.5 eV, The (PL) results exhibited prominent peaks with a central wavelength of 456, 458, 458, 464, and 466 nm. Additionally, the PL intensity of the Ag–WO$_3$-NP samples increased proportionally with the concentration of the core. Furthermore, the redshift seen at the peak of the PL emission band may be attributed to the quantum confinement effect. EDX analysis can verify the creation process of the Ag–WO$_3$ core–shell nanostructure. XRD analysis confirms the presence of Ag and WO$_3$ (NPs). The TEM images provided a good visualization of the core-spherical shell structure of the Ag–WO$_3$ core–shell NPs. The average size of the particles ranged from 30.5 to 89 (nm). The electrical characteristics showed an increase in electrical conductivity from (5.89×10^{-4}) (Ω cm)$^{-1}$ to (9.91×10^{-4}) (Ω cm)$^{-1}$, with a drop in average activation energy values of (0.155 eV) and (0.084 eV) at a concentration of 1.6 µg/mL of silver.

Core–shell nanocomposites (NCs) have garnered significant interest in recent years due to their exceptional structural, chemical, photocatalytic, physical, and optical characteristics[1–7]. Core–shell NCs have a significant coupling exciton effect that exists between the core (noble metal) with surface plasmon resonance (SPR) characteristics and the excitons of the semiconductors (shell)[8–10]. A variety of methods have been documented for producing core–shell NPs. The wet chemistry approach involves the interaction between the core or shell material and the surrounding liquid, resulting in the formation of core–shell structures. Although this process does produce a substantial outcome, it is occasionally deemed unsustainable due to the use of hazardous substances. In contrast, physical approaches provide several benefits in comparison to wet chemical procedures. Additionally, physical approaches need little sample preparation and do not necessitate the use of environmentally toxic chemicals. The physical techniques include several approaches, such as heat flow tubes, flame assembly, spray pyrolysis techniques, and plasma procedures[11]. The aforementioned techniques are implemented to generate core–shell nanoparticles in a relatively brief amount of time. Laser ablation is regarded as one of the physical methods within this context. Laser ablation has been used in many methodologies for the synthesis of core–shell nanoparticles, such as laser ablation in the presence of a reactive gas and laser ablation in a liquid medium[12].

[1]Applied Science Department, University of Technology-Iraq, Baghdad, Iraq. [2]Laser and Optoelectronic Department, University of Technology-Iraq, Baghdad, Iraq. [3]Institute of Laser for Postgraduate Studies, University of Baghdad, Baghdad, Iraq. [4]Electrical Engineering Department, Northern Border University, Arar, Saudi Arabia. [5]Al-Farahidi University, Baghdad, Iraq. ✉email: evan_tarq@yahoo.com; evan.t.salim@uotechnology.edu.iq; mokaram_76@yahoo.com; makram.a.fakhri@uotechnology.edu.iq; ahmad.azzahrani@nbu.edu.sa

Yellow powdered tungsten oxide (WO3) has a density of 7.16 g/cm^3, a melting point of 1473 °C, and a boiling temperature of 1700 °C. While it is insoluble in water and most acids (apart from hydrofluoric acid), it is soluble in ammonium hydroxide, where it forms tungstate[13–17]. Tungsten oxide (WO_3) has a narrow bandgap ranging from 2.7 to 3.1 (eV), making it a material with notable reactivity within the visible light range. Tungsten trioxide (WO_3) exhibits stable semiconductor properties[18,19]. Due to its unusual physicochemical characteristics, it has the potential to be used in a variety of technical domains, including lithium-ion batteries[20,21], solar energy devices, photocatalysts[16,22], smart windows, electronic information displays and electrochromic devices[23–29]. While WO3, ZnO, and SnO are commonly employed as gas sensor applications, Tungsten, specifically, has the capability to detect gases that are toxic and destructive, such as NO2, Acetone, and NH3[16,30], H2S, and hydrocarbons such as carbon monoxide, such as benzene and methane[31–33]. Thus, the production of WO3 is important. However, WO3 is not widely available due to price rises and export limitations imposed by manufacturing countries[34]. The extremely common semiconductor metal oxides used in optoelectronic devices include WO3, MoO3, SnO2, TiO2, and ZnO. Surprisingly, among all these, WO3 is used in many electronic devices due to its tunable properties of high thermal stability, visible-range optical absorption, surface morphology, and chemical composition[35,36]. Extensive research has been conducted on the plasmonic properties shown by silver (Ag) NPs, primarily owing to their exceptional performance relative to other surface plasmon resonance (SPR) metals throughout the visible region of the electromagnetic spectrum. Silver (Ag) nanostructures exhibit distinct, strong, and precise plasmonic phenomena within the visible region of the electromagnetic spectrum. Moreover, localized surface plasmon resonance (LSPR) may manifest in silver (Ag) nanostructures measuring less than 5 nm in size[37–40]. The core–shell nanostructures provide many benefits. By altering the material composition, core/shell size ratio, and the surrounding medium, it is possible to adjust and combine the plasmonic response of the nanoparticles. The control of nanostructured materials has garnered significant attention in recent years due to the possible properties that may be achieved and manufactured. These materials possess versatile properties that make them suitable for several application domains, including but not limited to biological, optical, magnetic electronic fields and electrical[10,41–49]. Numerous fields of study have developed an interest in nanoscience. Consequently, it is essential to produce nanoparticles with the ideal size distribution, morphology, and crystallinity[50]. Many controlled synthesis techniques for Ag-NPs, including biosynthesis, evaporation condensation, sol–gel, laser ablation, microwave processing, electron irradiation, electrochemical and photochemical have been documented[51,52]. Every approach has both benefits and drawbacks[53–57]. Nevertheless, every technique can be categorized into one of two methodologies: bottom-up or top-down. Recent studies have shown that the pulsed laser ablation in liquid medium technique (PLAL) is an effective and promising method for regulating the particle size of nanostructured materials that are manufactured[58]. The underlying principle of this technique is the use of high-intensity pulsed laser ablation to initiate a laser-matter interaction on the surface of the object under examination. This interaction results in the generation of a plasma plume that is fully submerged in a liquid medium[59–65]. This phenomenon results in the establishment of a unique thermodynamic condition characterized by elevated pressure levels. The generation of nanoscale particles is facilitated by the creation of distinctive thermodynamic conditions characterized by elevated levels of pressure and temperature[64,66]. The PLAL processes have the potential to generate nanostructured materials in an extensive range of shapes and dimensions. PLAL, which stands for metal or metal oxide-NCs, has recently been acknowledged as the most adaptable, promising, and straightforward technique for producing such materials. An instance of the effective use of the Nd:YAG laser is the creation of Ag nanoparticle-decorated carbon nanotubes (CNTs) to enhance the photocatalytic efficacy in the removal of naphthalene from[67–79] water[80] and MWCNTs/Ag NCs for catalytic degradable material for nitro compounds and dyes[81]. The PLAL process has many benefits, including simplicity, low cost, a decrease in by-product generation, the absence of catalyst and vacuum requirements, high-purity nanomaterial manufacturing, and precise control over particle shape and size by modifying laser settings. The metal-oxide core–shell architecture offers several benefits in terms of enhanced stability against sintering[82] and leaching[83], the potential to impart magnetic properties to the NCs[84,85], and, notably, the ability to modify the material's electronic structure through metal-oxide interactions[86]. Charge transfer is a critical factor in determining the physicochemical, spectroscopic, and catalytic characteristics of the NCs materials[87–89]. By modifying their structure (e.g., shell thickness and core size) and composition (e.g., alloying the core or doping the shell), metal-oxide Nc can enable one to adjust their properties due to the multitude of interactions observed within them[90–92]. Consequently, the characteristics of metal-oxide core–shell NCs are unlike those of any other material[93,94]. The Ag–WO$_3$ NPs are of particular interest for several reasons. Firstly, the Ag (NP) core can effectively generate strong localized surface plasmons (LSP) across the visible spectrum. Secondly, the LSP can be optimized by adjusting the core (Ag-NPs) diameter. Thirdly, WO$_3$ itself is an excellent gas sensor material. Fourthly, the Ag–WO$_3$ core–shell NPs are expected to function as a good Schottky junction sensor. Fifthly, the well-known layered structure of WO$_3$ at nanometer thickness may enhance the sensor performance through quantum effects. Lastly, the combination of the core (Ag-NPs) and the layered WO$_3$ shell could lead to the development of a new generation of gas sensors with enhanced quantum effects. This work aimed to produce Ag–WO$_3$ core–shell nanoparticles utilizing a laser ablation approach in deionized water at normal room temperature. The XRD, UV–Vis spectrum, PL, EDX, FE-SEM, and TEM techniques were used to analyze the structure, morphology, optical, and electrical features of Ag–WO$_3$ core–shell NPs generated at different core concentrations. Additionally, the room-temperature electrical properties of these NPs were also examined.

As a novel contribution, this work presents a manipulation and fine-tuning of the optical and electrical properties of Ag–WO$_3$ core–shell nanoparticles by varying the Ag core concentration employing laser ablation in liquid technique, the study showcased the impact of core concentration on the structural, morphological, optical, and electrical characteristics of Ag–WO$_3$ core–shell nanoparticles.

Experimental work

We have synthesized Ag–WO$_3$ core–shell NPs by a two-step process of laser ablation in water. Initially, a 1064 nm Nd:YAG pulsed laser beam was used to ablate a square silver target plate with dimensions of (0.8*0.8 mm) and high purity of (99.9%) that was submerged in 3 ml of distilled water inside a glass container without the use of any chemical additives. A repetition rate of 1 Hz, 10 focal length of the lens and a pulse width of 15 ns were used. The silver target was cleaned before immersion and irradiation by dipping it in acetone and washing it in pure water. The laser ablation procedure was conducted on the Ag target using a laser fluence of 6.12 J/cm^2 and number of laser pulses (200, 250, 300, 350, and 400). The experiment was conducted at different concentrations of silver. Resulting in the production of nanoparticles in the form of a suspension (0.36, 0.76, 1.2, 1.6, and 1.96 μg/mL). Step two, the silver target was subsequently substituted for a tungsten target in the solution, to produce the Ag–WO$_3$ colloidal core–shell. Using 1064 nm, 1 Hz, 10 focal length lens with a constant laser fluence of 76.34 J/cm^2 laser pulses (300), respectively. Figure 1 illustrates the schematic diagram depicting the process of forming Ag–WO$_3$ core-Porous shell NPs by laser ablation in water (Table 1). Figure 2 depicts an image of newly formed colloidal Ag–WO$_3$ core–shell NPs. It is evident that increasing the number of laser pulses caused an increase in core concentrations and change in the color of the solution, transitioning from light yellow to deep yellow. This change in color indicates a variation in particle size according to the number of laser pulses. The concentrations of the Ag colloidal nanoparticles were determined by estimating the weight of the Ag target before and after ablation by laser. The concentration was estimated as a function of the laser pulses number using a five digit (digital scale) precision weighing instrument that can measure weight to an accuracy of 0.00001 g. The following formulae were used. Five distinct concentrations of (Ag) nanoparticles where used[95–97].
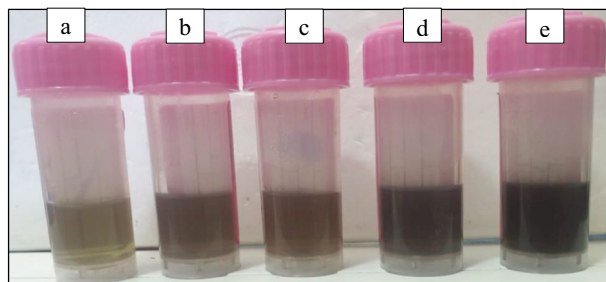
$$\Delta M = (m_1 - m_2)\,\mu g \tag{1}$$
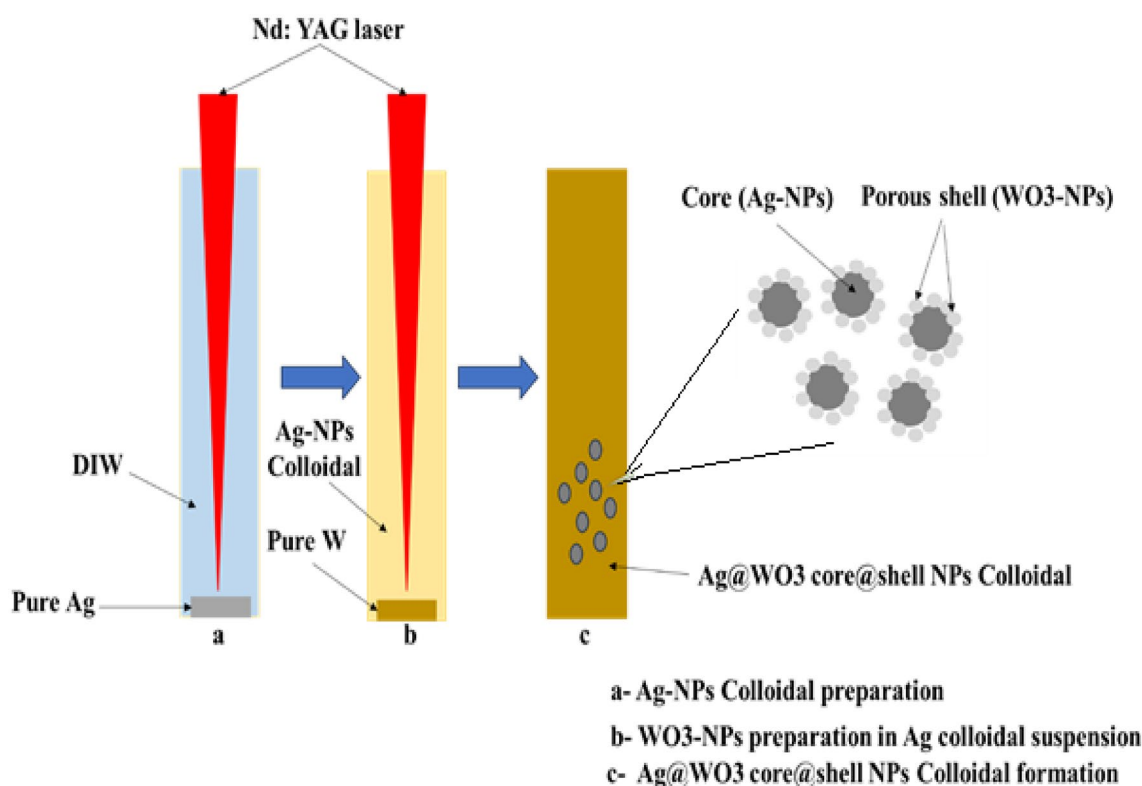
Figure 1. Schematic diagram illustrating the process of forming Ag–WO$_3$ core-Porous shell NPs using pulsed laser ablation in water.

Sample	Laser pulses	Concentrations (μg/mL)
1	200	0.36
2	250	0.76
3	300	1.2
4	350	1.6
5	400	1.96

Table 1. Explained different concentrations of colloidal silver versus number of laser pulses.

Figure 2. Photograph of freshly prepared colloidal Ag–WO$_3$ core–shell NPs at different concentrations of Ag (a—0.36, b—0.76, c—1.2, d—1.6, e—1.96) μg/mL.

where: m$_1$ and m$_2$ denote the target's mass prior to and subsequent to ablation, respectively. The formula for calculating the concentration is as follows[98–100]:

$$C = \Delta M(\mu g)/V(m_l) \tag{2}$$

where: V stands for the liquid's amount.

In order to study the structural characteristics of Ag–WO$_3$ core–shell NPs deposited on silicon substrate, XRD measurement was used (XRD-6000, Shimadzu, X-ray diffractometer). In this work, all samples were processed using the FE-SEM (ARYA Electron Optic) equipment, which featured an energy dispersive X-ray (EDX), to accomplish the advantages indicated before. The TEM (type CM10 pw6020, Philips-Germany) was used to analyze the size and form of Ag–WO$_3$ core–shell NPs. Using a UV–Vis double beam spectrophotometer (Shimadzu UV-1800), the optical absorbance of the colloidal nanoparticles solution was documented. We measured the resistance (R) values of the Ag–WO$_3$ core–shell samples using a Kiethly electrometer and an excitation wavelength of 325 nm, as part of the Pl analysis.

Results and discussion

The optical properties and the energy gap of the Ag–WO$_3$ core–shell NPs were determined by means of ultraviolet spectroscopy. The absorption spectrum of Ag–WO$_3$ core–shell NPs samples was obtained in Fig. 3 using a fluence of 76.43 J/cm^2, 400 laser pulses, and a wavelength of 1064 nm. The samples were prepared with varying concentrations of silver (0.36, 0.76, 1.2, 1.6, and 1.96 μg/mL) and a constant fluence of 6.12 J/cm^2. Figure 3 shows the optical absorption spectra of the Ag–WO$_3$ core–shell nanoparticles that were produced by employing pulse
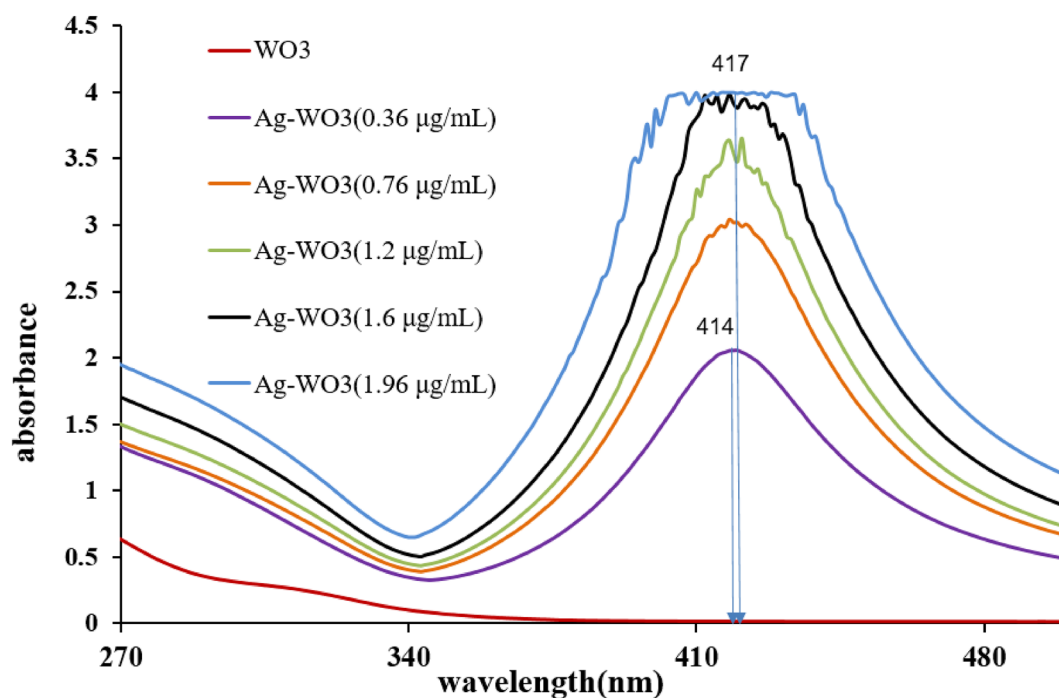
Figure 3. Absorption spectrum of Ag–WO$_3$ nanoparticles with various Ag nanoparticle concentrations.

laser ablation in water. The number of laser pulses used in the synthesis process varied between 200, 250, 300, 350, and 400. A strong plasmonic absorption peak at 410 nm is easily discernible in the absorption spectra of Ag–WO$_3$ core–shell nanoparticles. The spectrum exhibited distinct and broad absorption peaks in the visible region, located at approximately 414, 416, 415, 417, and 417 nm for the samples with concentrations of 0.36, 0.76, 1.2, 1.6, and 1.96 μg/mL, respectively. In agreement with one of the previous studies[101,102]. The intensities of all distinctive peaks, which were seen in the Ag–WO$_3$ NPs samples, exhibit an increase when the amounts of silver particles are increased. The observed peaks ascribed to the presence of Ag-NPs. Furthermore, it was observed that there were minor absorption peaks at around 311, 312, 313, 314, and 315 nm, indicating the presence of WO$_3$ nanoparticles for the samples with concentrations of 0.36, 0.76, 1.2, 1.6, and 1.96 μg/mL, respectively. After the incorporation of Ag NPs into WO$_3$ NPs, the absorption band edge of bare WO$_3$ is redshifted (toward a longer wavelength). The presence of both peaks provided evidence for the creation of the Ag–WO$_3$ core shell NPs[103–105]. This result gives a clear indication of the effect of Ag nanoparticles due to the effect of SPR coming from Ag (core) nanoparticles. Consequently, the bandgap energy of the material decreased as a result of the redshifted of absorption band edges produced by the incorporations of Ag NPs. The band gaps of the samples at different concentrations of silver (0.36, 0.76, 1.2, 1.6, and 1.96 μg/mL) are presented in Fig. 4. The optical
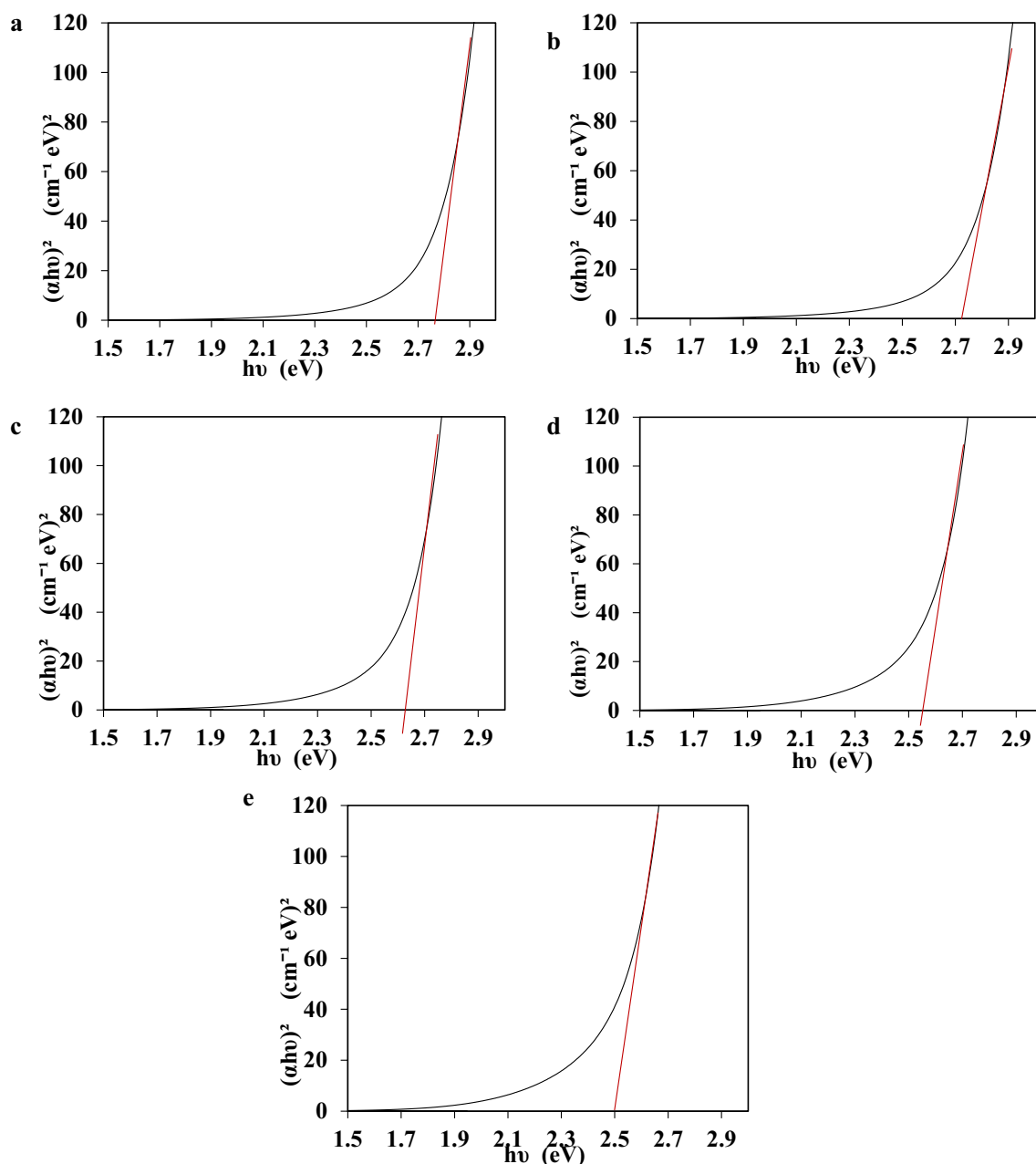
Figure 4. The absorption and energy gap spectra of Ag–WO$_3$-NPs at different concentrations of Ag (**a**—0.36, **b**—0.76, **c**—1.2, **d**—1.6, **e**—1.96) μg/mL.

absorption band gap follows a power law when incident photon energy is greater than the band gap and above the exponential[106–109]:

$$(\alpha h\nu) = \beta \left(h\nu - E_g \right)^n \qquad (3)$$

where E_g is the optical bandgap, α is the absorption coefficient, n is an exponent, β is the edge with parameter and $h\nu$ is the incident photon energy.

It can be observed from Fig. 4 that the optical band gap energy decreases to 2.75, 2.73, 2.62, 2.55, and 2.5 eV as the concentration of Ag increases. These values are very close to those stated in a previous study[110], the band gap tailoring in core–shell NPs was attributed to its shape and the quantum confinement effect[111,112]. The interfaces of Ag–WO$_3$ NPs have a significant impact on the processes of charge transfer and separation[113,114]. This is attributed to the presence of Ag NPs, which function as localized surface plasmons (LSP). This process credits the combination of electromagnetic waves to the oscillations of electrons[115]. This procedure enables the reduction of the band gap in the core cell structure. As a result, the adjusted band gap allows for increased interaction between visible light and the core–shell compared to the regulated WO$_3$. The core–shell has promising optical and electrical properties because to its ability to fine-tune the band gap features[116,117]. Consequently, the bandgap energy of the material decreased as a result of the redshifted of absorption band edges produced by the incorporations of Ag NPs.

The flat peak in surface plasmon resonance typically refers to the collective oscillation of electrons at the interface between a metal and a dielectric material when excited by incident light. The resonance condition occurs when the momentum of incident photons matches the momentum of the surface plasmons.

The SPR response may not exhibit a sharp peak, making it challenging to identify the resonance position. This could be due to various factors, such as broadening of the SPR peak due to particle size distribution, polydispersity, or other experimental conditions.

Figure 5 displays the photoluminescence (PL) spectrum of core–shell NPs consisting of silver (Ag) and tungsten oxide (WO$_3$). The photoluminescence (PL) studies revealed increased intensities in all the Ag–WO$_3$ samples created using varying amounts of silver (0.36, 0.76, 1.2, 1.6, and 1.96 µg/mL). The spectrum shows excitation bands located at 456, 458, 458, 464, and 466 nm, which correspond to energy gaps of about 2.71, 2.7, 2.7, 2.67, and 2.66 eV, respectively. The energy gap value approximated using PL data is marginally greater in magnitude compared to what was ascertained using UV–vis data[118]. Further, it differs from the energy gap of pure WO$_3$. The PL intensities of the Ag–WO$_3$ NPs peaks exhibited a significant increase compared to the PL peak of WO3. Additionally, these peaks show a minor shift, which may be ascribed to the enhanced photoluminescence seen in the NCs structure. This improvement is due to the incorporation of Ag-NPs. These results are consistent with UV–visible results. Ag–WO$_3$ CS-NPs' emission energy and PL emission wavelength are displayed in Table 2 as a function of Ag concentrations.

Figure 6 displays the diffraction peaks corresponding to the core–shell samples. These peaks were generated using a fluence of 76.34 J/cm^2 and 400 laser pulses. The figure also displays a wavelength of 1064 nm with different concentrations of silver (0.36, 0.76, 1.2, 1.6, and 1.96 µg/mL). This figure further displays the prominent peaks that can be ascribed to hexagonal WO$_3$, as indicated by the JCPDS card number 00-33-1387 and PDF number #75-2187. The peaks are located at 2θ values of 25.5° and 58.84°, corresponding to the orientations (110) and (220), respectively. On the other hand, the peak at 2θ = 83.4o with orientations (223), indexed to JCPDS card no. 89-1287, is related to the tetragonal WO$_3$ phase. The presence of Ag-NPs was verified by the peaks at 2θ = 38.2o, 44.3o, 64.5o, and 77.86o with orientations (111), (200), (223), and (311). This can be attributed to cubic Ag
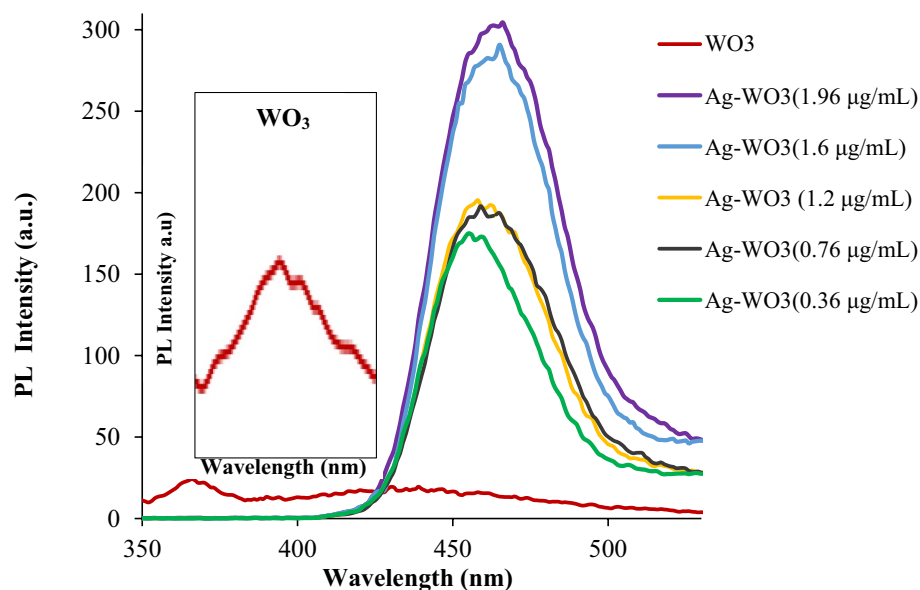
Figure 5. PL spectrum of Ag–WO$_3$ nanoparticles with various Ag nanoparticle concentrations.

Ag concentrations (µg/mL)	UV–vis energy gap (eV)	PL	
		Emission peak wavelength (nm)	Band gap energy (eV)
0.36	2.73	456	2.71
0.76	2.72	458	2.7
1.2	2.6	458	2.7
1.6	2.55	465	2.67
1.96	2.5	466	2.66

Table 2. The Ag–WO$_3$ core–shell NPs' emission energy and PL emission wavelength as a function of Ag concentrations.
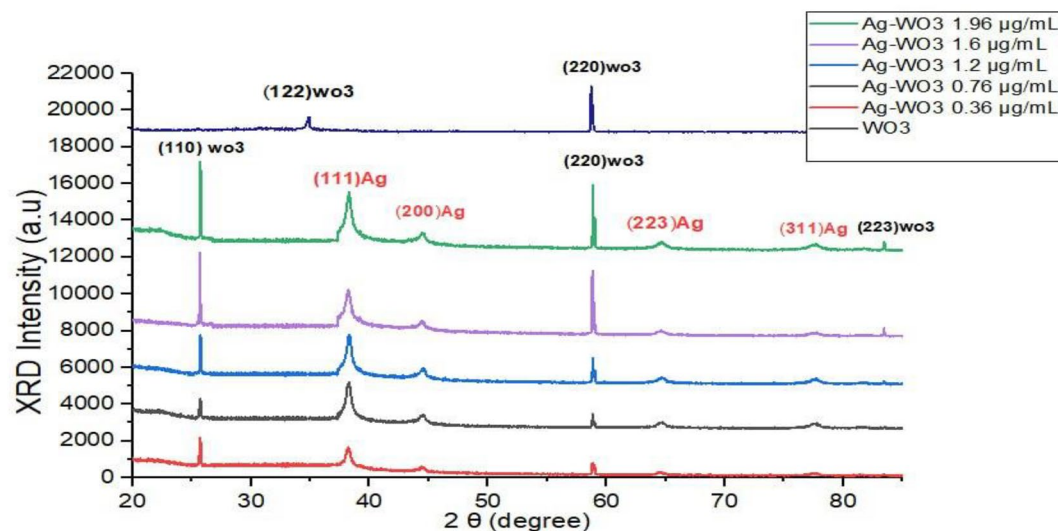
Figure 6. XRD patterns of Ag-–O$_3$ nanoparticles using various Ag concentrations.

nanoparticles, according to pdf number 870720. Due to the relatively high diameter of the core, significant diffraction peaks are generated. XRD identification of the core–shell configuration[119–121] showed that these results are in line with the study[122]. When exposed to X-ray radiation, the greater concentrations of aggregated silver nanoparticles resulted in a greater degree of reflection[123,124]. For the WO$_3$ sample, two peaks appeared at 2θ: 28.92° and 58.84°. While 28.92° corresponds to the (122) plane according to (JCPDS # 201323) triclinic WO$_3$ phase structure, 58.84° corresponds to the (220) plane hexagonal WO3 phase structure. In addition, the XRD patterns of Ag–WO$_3$ core/shell NPs exhibit a marginally greater intensity than those of shell NPs (Fig. 6). This may be the result of incorporation Ag core NPs causing an increase in particle size and crystallinity. Table 3 illustrates

Ag concentration µg/mL	2θ	FWHM	Miller indices	Crystalline size (nm)	Dislocation density (δ)	Microstrains
0.36	25.5° 58.84°	0.146 0.114	110 220	55.45 63.43	0.078227463 0.038693379	0.062103798 0.043311681
0.76	25.5° 58.84°	0.13 0.093	110 220	56.86 72.82	0.729303684 0.033897991	0.063672181 0.04971665
1.2	25.5° 58.84° 83.4°	0.129 0.089 0.235	110 220 223	62.76 81.25 26.384	0.069118786 0.030207989 0.063461585	0.054872534 0.033813505 0.076545193
1.6	25.5° 58.84° 83.4°	0.121 0.083 0.224	110 220 223	66.91 85.19 27.67	0.064832349 0.02783208 0.06049102	0.052469586 0.031154016 0.072962227
1.96	25.5° 58.84° 83.4°	0.11 0.081 0.211	110 220 223	73.60 89.28 29.38	0.046790533 0.030774089 0.068727812	0.050938499 0.027492664 0.056980402

Table 3. XRD parameters of core–shell Ag@WO$_3$ nanoparticles prepared with various Ag nanoparticle concentrations.

the grain size, dislocation densities, Miller indices, and micro strains of Ag–WO$_3$ nanoparticles. The Scherrer formula is used to calculate the size of crystallites[125–127]:

$$D = k\lambda/(\beta \cos \theta) \quad (4)$$

where λ is the X-ray wavelength, β is the full width at the half maximum, k is the constant 0.89 < k < 1 change with Miller indices and crystallite shape, but is frequently close to 0.94, and θ is the diffraction angle[128–130]. The dislocation density was calculated using the formula (3) and the Microstrains were determined using Eq. (5). The table demonstrates a small augmentation in crystalline size when the concentration of silver particles is increased. Conversely, the dislocation density and Microstrains exhibited a reduction due to the aforementioned factor. The dislocation density in lines/m2 can be determined by employing the equation[131–133]:

$$\delta = 1/D2_{XRD} \quad (5)$$

(d) Lattice strain or Microstrains (η).

The lattice strain is caused by lattice imperfections such dislocations, vacancies, interstitials, and substitutional. These defects cause the atoms to be displaced from their original places in the crystal structure, as a result, the lattice plane d-spacing may be varied. Microstrains will occur during the production of the thin film. This strain may be estimated using the equation below[134–137].

$$\eta = \beta/4 \tan(\Theta) \quad (6)$$

The film deposition circumstances will have an impact on structural factors such grain size, crystallinity, and crystal structure.

Figure 7 shows the FESEM images of Ag–WO$_3$ core–shell NPs samples as function of Ag-NPs concentrations. The Ag-NPs concentrations in the samples varied from 0.36 to 1.96 μg/mL. As seen in Fig. 7. The Ag–WO$_3$ core–shell structure displays a noticeable augmentation in particle size as the concentration of silver increases. Furthermore, the particles have a well-defined spherical morphology that aligns precisely with the findings of the study[138–140]. The shape, size and agglomerated particles of nanoparticles are determined by the concentrations of Ag-NPs, as seen in Fig. 7. Specifically, the size of WO$_3$ outer shell nanoparticles rises proportionally with higher concentrations of Ag-NPs. Additionally, the size of the Ag core also increases in tandem with the Ag-NPs concentrations. This aligns with the findings reported in a prior investigation[141]. The (SEM) images reveal the presence of core/porous-shell structures in the microspheres. The pores inside the shell are densely and uniformly distributed, as seen from the distinct color difference. The shell exhibited a high degree of porosity and was characterized by its minimal thickness. The pictures given below depict various morphological characteristics of both the core and the shell layer. The outer layer, WO$_3$, has a higher degree of surface roughness in comparison to the inner layer, Ag.
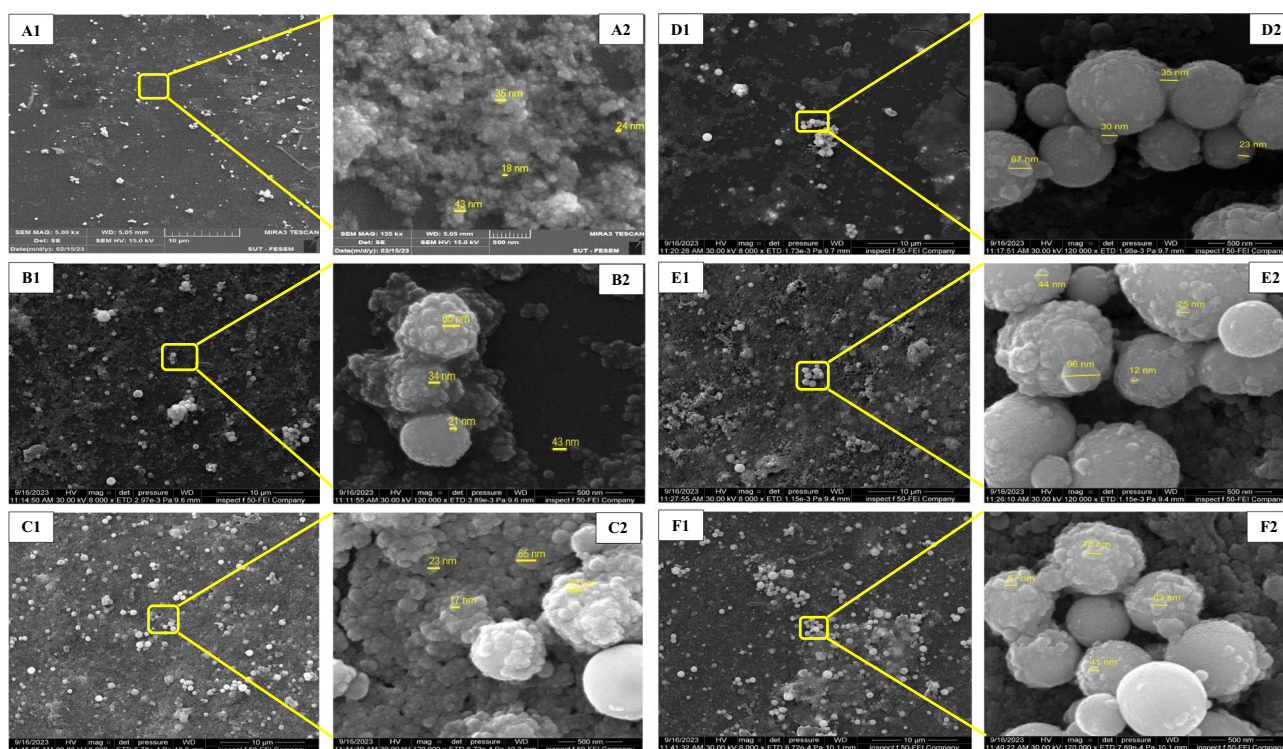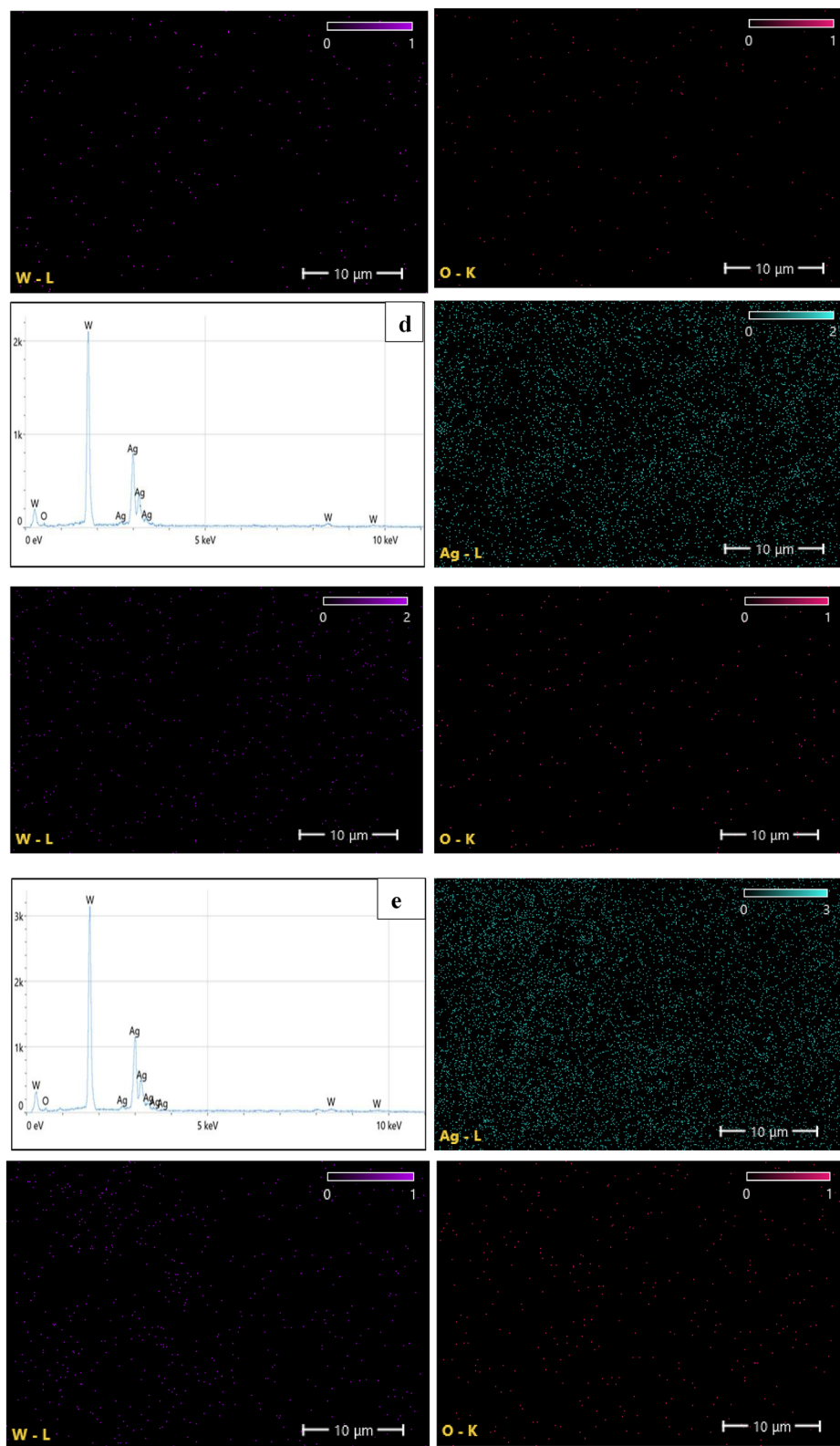

Figure 7. FESEM images of (**a**) WO$_3$-NPs and Ag–WO$_3$-NPs at various Ag concentrations (**b**—0.36, **c**—0.76, **d**—1.2, **d**—1.6 and **e**—1.96) μg/mL.
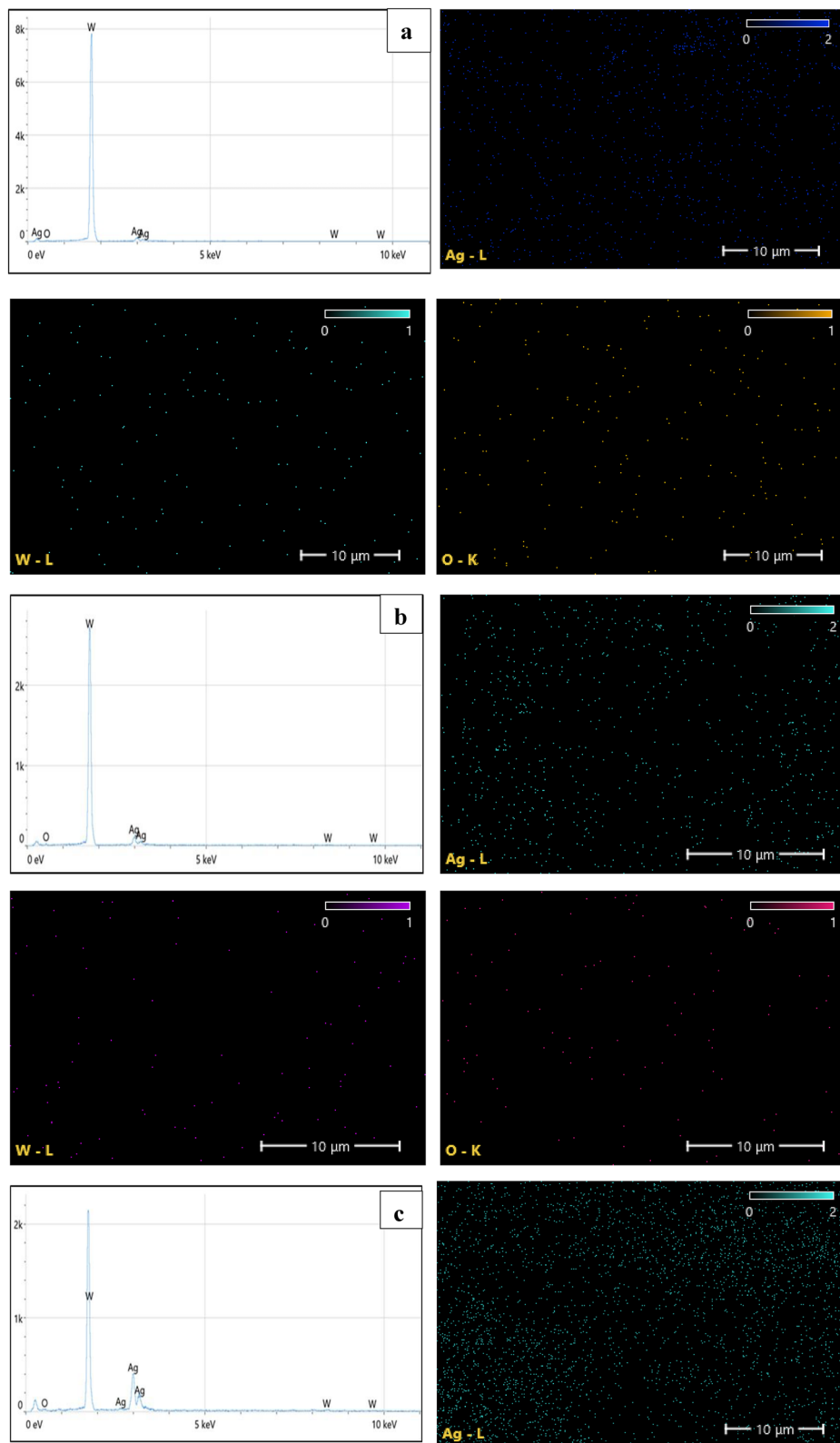
Figure 8. EDX spectra and elemental mapping images for Ag–WO$_3$ nanoparticles for various Ag concentrations (**a**—0.36, **b**—0.76, **c**—1.2, **d**—1.6, and **e**—1.96) μg/mL.

Figure 8. (continued)

The EDX results for Ag–WO$_3$ core–shell nanoparticles are depicted in Fig. 8. EDX analysis has the potential to provide insights into the formation process of the Ag–WO$_3$ core–shell nanostructure. It can give an indication for the formation of the Ag–WO$_3$ core–shell nanostructure, according to Muhammad A. Imam and Nitin

Chopra[142,143]. The presence of tungsten (W), oxygen (O), and silver (Ag) in the core shell system was confirmed by this figure. Supporting the EDX results of Ag–WO$_3$ core–shell NPs, Fig. 8a,e illustrate the mapping outcomes of Ag, WO$_3$, and O, respectively. Ag NPs showed high intensity in EDX due to the increase laser pulses and increasing Ag concentration. Table 4 illustrates the weight percentages of the elements contained in the samples, as well as the stoichiometries of WO$_3$. The stoichiometric ratio and weight percentage appear to exhibit an upward trend when the concentration of silver nanoparticles increases.

Figure 9a–e depicts transmission electron microscopy (TEM) pictures of Ag–WO$_3$ core–shell NPs samples, illustrating the relationship between the concentration of silver and the observed characteristics. The form and size of NPs are influenced by the concentration of silver, as depicted in the figure. The size of the silver core exhibits a positive correlation with the concentration of silver. In this study, the transmission electron microscopy (TEM) images demonstrate the production of Ag nanoparticles of varying sizes, as well as the presence of some

Ag concentration µg/mL	W %	Ag %	O %	WO$_3$ Stoichiometry (%)
0.36	31.2	27.0	41.8	19
0.76	32.2	29.4	38.4	22
1.2	32.6	33.0	34.4	24
1.6	35.0	42.2	22.8	41
1.96	35.2	44.6	20.2	45

Table 4. Ag–WO$_3$-NPs stoichiometry and weight percent of elements.
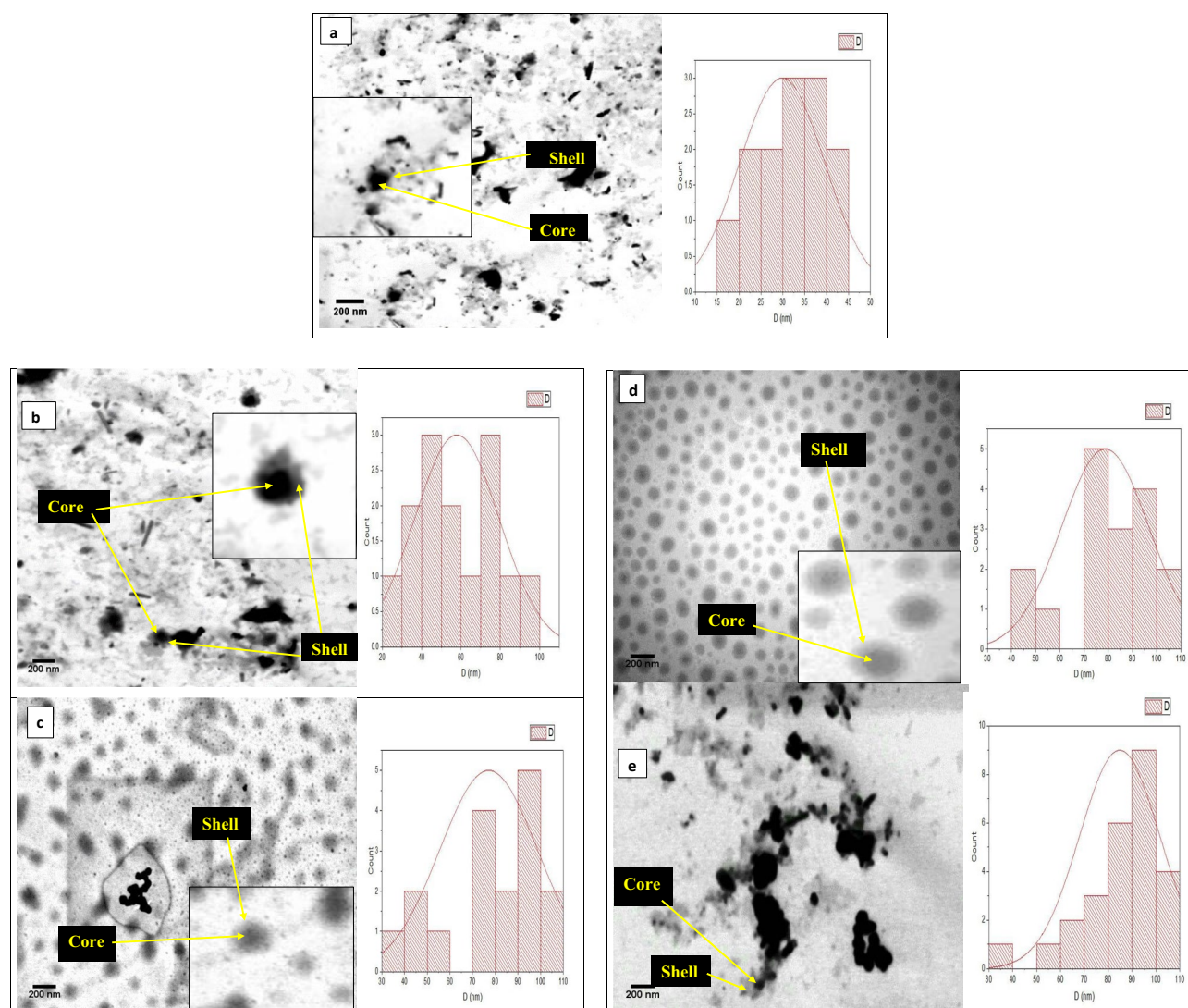
Figure 9. TEM images of Ag–WO$_3$-NPs with different Ag concentrations (**a**—0.36, **b**—0.76, **c**—1.2, **d**—1.6, and **e**—1.96) µg/mL.

monodisperse Ag particles that are enveloped by a WO3 shell. Additionally, the presence of both aggregated and agglomerated silver particles was noted as increasing the concentration of silver. This matches what was stated in the results of the FE-SEM. Besides, these pictures provide confirmation that the central Ag particles possess spherical morphologies. Table 5 presents data on the average particle size of Ag–WO$_3$ core–shell and Ag core. The results indicate that when the concentration of silver nanoparticles was raised from 0.36 to 1.96 μg/mL, the particle size of the Ag–WO$_3$ core–shell climbed from 30.5 to 89 nm, while the size of the Ag core increased from 28 to 81 nm. Thus, the manipulation of core size is a viable approach for modulating the overall dimensions of metal-oxide nanoparticles, hence exerting a significant influence on the characteristics of the resulting nano-composites. This is consistent with what was reported in these studies[144–146].

Electrical measurements of WO$_3$ NPs and Ag–WO$_3$ core–shell samples at various Ag concentrations (0.36, 0.76, 1.2, 1.6, and 1.96 μg/mL) were studied in order to achieve the optimum sample conductivity (lowest resistance). The relation of resistance (R) as a function of temperature (T) was determined, as shown in Fig. 10. The reported resistance values of the Ag–WO$_3$ core–shell were high at low temperatures and gradually decreased as the temperature of each sample increased. This is the typical situation for semiconducting materials, as they possess a temperature coefficient that is negative (wherein the resistance decreases as the temperature increases). At thermal equilibrium conditions (room temperature), the initial reading was obtained for each sample to evaluate the resistivity of Ag–WO$_3$ manufactured at different Ag concentrations. As shown in this figure, the sample prepared with a concentration of 1.6 g/mL of silver yielded the lowest resistance of approximately 47.1 MΩ at 150 °C. The electrical resistance of the created samples was reduced on a regular basis as compared to the WO3 sample. Because (Ag) nanostructures are metals characterized by elevated levels of free carriers, the conductivity (σ) was raised.

Figure 11 shows the logarithmic conductivities (lnσ) of the carrier's curve as a function of reciprocal temperature (1000/T) for WO$_3$ and Ag–WO$_3$-produced samples with various Ag concentrations (0.36, 0.76, 1.2, 1.6, and 1.96 μg/mL). The corresponding electrical conductivities (σ) of the samples were determined using the equation[147–149]:

$$\sigma = \frac{1}{\rho}(\delta\,cm)^{-1} \tag{7}$$

The equation shows the resistivity (ρ) in (Ω cm). Based on the figure, the electrical conductivity of the Ag–WO$_3$ core–shell increases as the concentration of silver increases. This rise in conductivity was due to an

Ag concentration (μg/mL)	Ag core size (nm)	Average particle size of Ag–WO$_3$ NPs (nm)
0.36	28	31
0.76	42	45
1.2	60	65
1.6	69	74
1.96	81	89

Table 5. Presents the average particle size of Ag–WO$_3$-NPs.
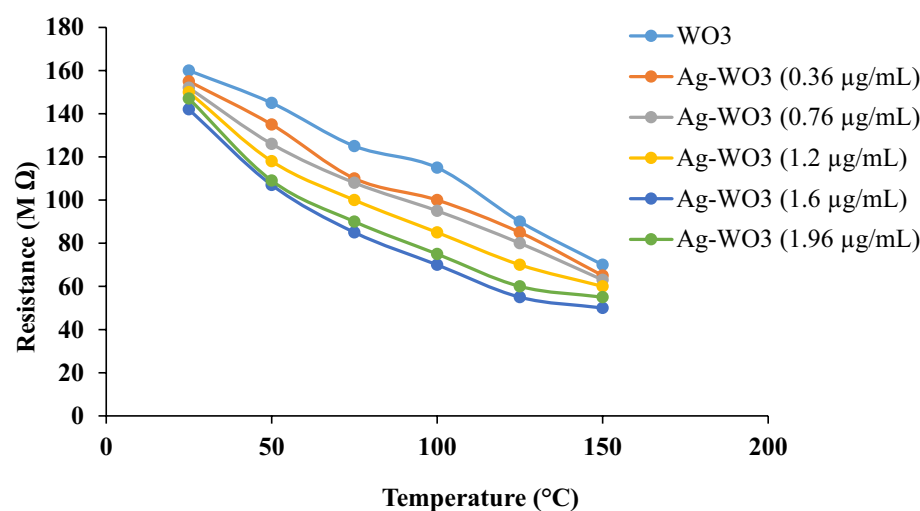
Figure 10. Temperature-dependent resistance of WO$_3$ NPs and Ag–WO$_3$ core–shell synthesized with various Ag concentrations.
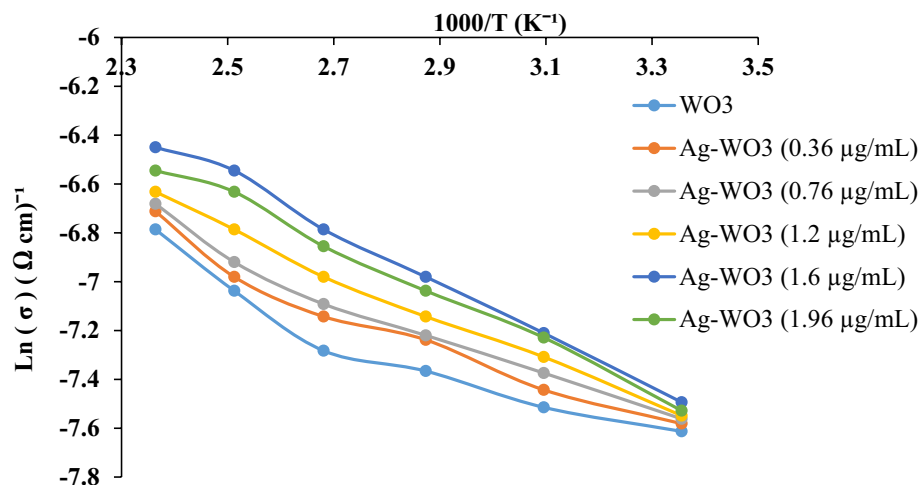
Figure 11. Arrhenius plot curve of ln (σ) versus (1000/T) of WO₃NPs and Ag–WO₃ core–shell synthesized with various Ag concentrations.

increase in carrier concentration and mobility[150], whereas the electrical conductivity (σ) values for the sample prepared with 1.96 µg/mL of silver were decreased. This result is due to the aggregation of (Ag) nanostructures in extremely high concentrations, which reduced the carrier mobility. The drop in mobility was directly proportional to the decrease in electrical conductivities[151–153]. This is consistent with what was stated in the previously work[154–156]. Table 6 show the activation energy of Ag–WO₃ with different Ag concentrations for current work and previous work[156,157].

The Arrhenius relation was used to calculate the activation energy[158–160]:

$$\sigma = \sigma^\circ \exp(-Ea/KT) \tag{8}$$

where the conductivities of carriers are denoted by the symbol σ, σ° represents the temperature of the independent portion conductivity, Ea denotes the necessary amount of energy for activation, then tn, constant of Boltzman (K), and the temperature, denoted by the letter T, is expressed as a value in Kelvin (k) unit. The activation energy values as a function of Ag concentration in the Ag–WO₃ samples are listed in Table 6.

The figure of merit (F.O.M.) of Ag–WO₃ core–shell samples created with various silver concentrations is displayed in Fig. 12. They were computed using Eq. (9) which was provided by Iles and Soclof[161–163]:

$$FOM = \frac{\sigma}{\alpha} \tag{9}$$

The absorption coefficient is represented by the symbol (α) and is the conductivity of electricity. The requirement for calculating the F.O.M. was to realize the optimal electrical conductivity (σ) as a function of the absorption coefficient (α) of Ag–WO₃ that was made by varying the amount of Ag (0.36, 0.76, 1.2, 1.6, and 1.96 µg/ mL). The concentration of 1.6 µg/mL of silver used in the preparation of the Ag–WO₃ core shell is considered a merit figure, as the incorporation of silver (Ag) was intended to improve the semiconductor material's properties.

Conclusion

We are successfully synthesizing a Novel Ag–WO₃ core–shell nanostructure using a two-step laser ablation process in deionized water. The impact of varying core concentrations (Ag-NPs) on the structural, electrical, morphological, and optical characteristics of Ag–WO₃ core–shell NPs have been investigated. XRD analysis has

Current work			Previous work[126]		
Ag concentration (µg/mL)	Average (σdc) (Ω cm)⁻¹	Activation energy (eV)	Time (s)	Ag concentration (µg/mL)	Average (σdc) (Ω cm)⁻¹
(0 Ag-(WO₃)	5.89×10^{-4}	0.155	5	6.328×10^{-8}	0.222
0.36	7.91×10^{-4}	0.117	15	8.5624×10^{-8}	0.221
0.76	8.25×10^{-4}	0.111	25	1.3619×10^{-7}	0.188
1.2	8.93×10^{-4}	0.094	35	3.4491×10^{-7}	0.220
1.6	10.6×10^{-4}	0.091	45	1.8557×10^{-7}	0.192
1.96	9.91×10^{-4}	0.084			

Table 6. The activation energy of Ag–WO₃ with different Ag concentrations for current work and previous work.
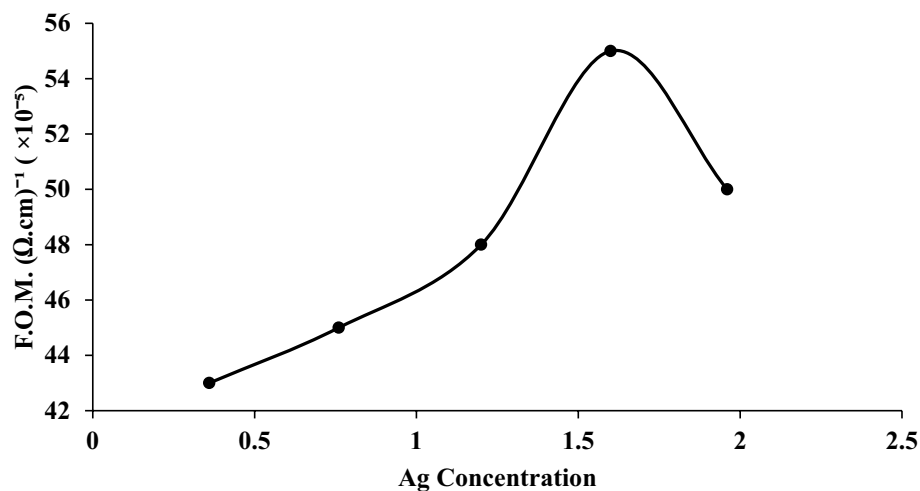
Figure 12. F.O.M. of Ag–WO$_3$ core–shell synthesized with various Ag concentrations.

confirmed the growth of a hexagonal polycrystalline WO$_3$ phase and the creation of cubic Ag-NPs. The presence of Ag–WO$_3$ core–shell NPs was verified using the XRD profile, which exhibited prominent diffraction planes. The transmission electron microscopy (TEM) analysis demonstrated that the size of the Ag core and the thickness of the WO$_3$ shell were dependent on the concentration of the core (Ag). Additionally, the study showed that the Ag–WO$_3$ nanoparticles exhibited a spherical morphology. The photoluminescence (PL) data exhibited a wide peak with a central wavelength of 456 nm. Following the creation of a hybrid Ag–WO$_3$ core–shell structure, the PL intensity of WO$_3$ was quenched. The wavelength of the absorption peak was abundantly evident at (414–417) nm. As a result of the increased ablation, the absorbance rose as the Ag-NPs concentration increased. A substantial decrease in the band gap was observed, with a transition from 2.73 to 2.5 electron volts (eV). The DC conductivity exhibited a distinctive semiconductor-like behavior, showing an increase with elevated temperatures. The figure of merit (F.O.M.) with the best performance was identified by an electrical conductivity observed at a concentration of 1.6 µg/mL of silver. The electrical conductivity of Ag–WO$_3$ has seen a notable increase, with the most advantageous characteristics due to the incorporation of Ag-NPs.

Data availability
Correspondence and requests for materials should be addressed to Evan T. Salim, Maryam S. Muhsin, Makram A. Fakhri.

References

1. Chaudhuri, R. & Paria, S. Core/shell nanoparticles: Classes, properties, synthesis mechanisms, characterization, and applications. *Chem. Rev* **112**, 2373–2433 (2012).
2. Chen, Y. *et al.* The study of surface plasmon in Au/Ag core/shell compound nanoparticles. *Plasmonics* **7**, 509 (2012).
3. Zamiri, R. *et al.* Laser assisted fabrication of ZnO/Ag and ZnO/Au core/shell nanocomposites. *Appl. Phys. A* **111**, 487 (2013).
4. Oh, J. & Kim, H. Synthesis of core–shell nanoparticles with a Pt nanoparticle core and a silica shell. *Curr. Appl. Phys* **13**, 130 (2013).
5. Wu, H. *et al.* Enhanced low-frequency microwave absorbing property of SCFs@ TiO2 composite. *Powder Technol.* **333**, 153 (2018).
6. Wu, H. *et al.* Co2+/Co3+ ratio dependence of electromagnetic wave absorption in hierarchical NiCo2O4–CoNiO2 hybrids. *J. Mater. Chem. C* **3**, 7677 (2015).
7. Wu, H., Wu, G. & Wang, L. Peculiar porous α-Fe$_2$O$_3$, γ-Fe$_2$O$_3$ and Fe$_3$O$_4$ nanospheres: Facile synthesis and electromagnetic properties. *Powder Technol.* **269**, 443 (2015).
8. Jiu, J. *et al.* Ag/TiO2 core–shell nanocables prepared with a one-step polyol process. *J. Nanopart. Res.* **14**, 1241 (2012).
9. Yu, Y., Qu, S., Zang, D., Wang, L. & Wu, H. Fast synthesis of Pt nanocrystals and Pt/microporous La$_2$O$_3$ materials using acoustic levitation. *Nanoscale Res. Lett.* **13**, 50 (2018).
10. Ismail, R. A., Mousa, A. M. & Amin, M. H. Synthesis of hybrid Au@ PbI2 core-shell nanoparticles by pulsed laser ablation in ethanol. *Mater. Res. Express* **5**(11), 115024 (2018).
11. Kim, K. S., Kim, D. J. & Zhao, Q. Q. Numerical analysis on particle coating by the pulsed plasma process. *Chem. Eng. Sci.* **61**(10), 3278–3289 (2006).
12. Han, H., Fang, Y., Li, Z. & Xu, H. Tunable surface plasma resonance frequency in Ag core/Au shell nanoparticles system prepared by laser ablation. *Appl. Phys. Lett.* **92**(2), 023116 (2008).
13. Chacon, C., Perez, M. R., Oskam, G. & Gattorno, G. R. Synthesis and characterization of WO3 polymorphs: Monoclinic, orthorhombic and hexagonal structures. *J. Mater. Sci. Mater. Electron.* **26**, 5526–5553 (2015).
14. Alwazny, M. S., Ismail, R. A. & Salim, E. T. High-quantum efficiency of Au@LiNbO3 core–shell nano composite as a photodetector by two-step laser ablation in liquid. *Appl. Phys. A* **128**, 500. https://doi.org/10.1007/s00339-022-05651-5 (2022).
15. Mukherjee, R., Kushwaha, A. & Sahay, P. P. Spray-deposited nanocrystalline WO$_3$ thin films prepared using tungsten hexachloride dissolved in NN dimethyl formamide and influence of in doping on their electron. *Mater. Lett.* **10**, 401–410 (2014).

16. Li, J., Liu, X., Cui, J. & Sun, J. Hydrothermal synthesis of selfassembled hierarchical tungsten oxides hollow spheres and their gas sensing properties. *ACS Appl. Mater. Interfaces* **7**, 10108–10114 (2015).
17. Fakhri, M. A. *et al.* Synthesis of LiNbO$_3$/SiO$_2$/Si nanostructures layer by layer based on Mach–Zehnder modulator using pulsed laser deposition route. *Silicon* **14**, 11781–11795 (2022).
18. Nagarjuna, R., Challagulla, S., Sahu, P., Roy, S. & Ganesan, R. Polymerizable sol–gel synthesis of nano-crystalline WO$_3$ and its photocatalytic Cr (VI) reduction under visible light. *Adv. Powder Technol.* **28**, 3265–3273 (2017).
19. Muhsin, M. S., Salim, E. T. & Saimon, J. A. Structural, morphological and optical properties of tungsten trioxide nanoparticle synthesis by pulsed laser ablation in water: Effect of laser fluence. *J. Opt.* https://doi.org/10.1007/s12596-023-01368-7 (2023).
20. Fakhri, M. A., Al-Douri, Y., Bouhemadou, A. & Ameri, M. Structural and optical properties of nanophotonic LiNbO$_3$ under stirrer time effect. *J. Opt. Commun.* **39**(3), 297–306 (2017).
21. Salmaoui, S. *et al.* Hexagonal nanorods of tungsten trioxide: synthesis, structure, electrochemical properties and activity as supporting material in electrocatalysis. *Appl. Surf. Sci.* **257**, 8223–8229 (2011).
22. Fakhri, M. A., Salim, E. T., Abdulwahhab, A. W., Hashim, U. & Salim, Z. T. Optical properties of micro and nano LiNbO$_3$ thin film prepared by spin coating. *Opt. Laser Technol.* **103**, 226–232 (2018).
23. Chen, H. J. *et al.* Gasochromic effect and relative mechanism of WO$_3$ nanowire films. *J. Chen. Nanotechnol.* **18**, 205701 (2007).
24. Hattori, Y. *et al.* Synthesis of tungsten trioxide nanoparticles by microwave plasma in liquid and analysis of physical properties. *J. Alloys Comp.* **560**, 105–110 (2013).
25. Fakhri, M. A., Salim, E. T., Wahid, M. H. A., Hashim, U. & Salim, Z. T. Optical investigations and optical constant of nano lithium niobate deposited by spray pyrolysis technique with injection of Li$_2$CO$_3$ and Nb$_2$O$_5$ as raw materials. *J. Mater. Sci. Mater. Electron.* **29**(11), 9200–9208 (2018).
26. Qin, Y. X., Wang, F., Shen, W. J. & Hu, M. Mesoporous threedimensional network of crystalline WO$_3$ nanowires for gas sensing application. *J. Alloys Comp.* **540**, 21–26 (2012).
27. Fang, L. *et al.* Tunable work function of a WO$_x$ buffer layer for enhanced photocarrier collection of pin-type amorphous silicon solar cells. *Appl. Phys. Lett.* **96**, 193501 (2010).
28. Abood, M. K., Salim, E. T. & Saimon, J. A. Niobium pentoxide thin film prepared using simple colloidal suspension for opto-electronic application. *Int. J. Nanoelectron. Mater.* **11**(2), 127–134 (2018).
29. Barczuk, P. J. *et al.* Structural and photoelectrochemical investigation of boron-modified nanostructured tungsten trioxide films. *Electrochim. Acta* **104**, 282–288 (2013).
30. Al-Douri, Y., Fakhri, M. A., Badi, N. & Voon, C. H. Effect of stirring time on the structural parameters of nanophotonic LiNbO$_3$ deposited by spin-coating technique. *Optik* **156**, 886–890 (2018).
31. Wang, L. *et al.* WO3 nanocubes: hydrothermal synthesis, growth mechanism, and photocatalytic performance. *J. Mater. Res.* **34**, 2955–2963 (2019).
32. Forbes, A. & Erasmus, R. M. Synthesis of tungsten oxide nanostructures by laser pyrolysis Bonex Wakufwa Mwakikunga Elias Sideras–Haddad and Gift Katumba Bathusile Masina. *Int. J. Nanopart.* **1**, 185–202 (2008).
33. Al-Douri, Y., Fakhri, M. A., Bouhemadou, A., Khenata, R. & Ameri, M. Stirrer time effect on optical properties of nanophotonic LiNbO$_3$. *Mater. Chem. Phys.* **203**, 243–248 (2018).
34. Arutanti, O. *et al.* Synthesis of composite WO$_3$/TiO$_2$ nanoparticles by flame-assisted spray pyrolysis and their photocatalytic activity. *J. Alloys Compd.* **591**, 121–126 (2014).
35. Shanmugasundaram, K., Thirunavukkarasu, P., Ramamurthy, M., Balaji, M. & Chandrasekaran, J. Growth and characterization of jet nebulizer spray deposited n-type WO$_3$ thin films for junction diode application. *Orient. J. Chem.* **33**(5), 2484 (2017).
36. Amir, H. A. A. A. *et al.* An investigation on GaN/ porous-Si NO$_2$ gas sensor fabricated by pulsed laser ablation in liquid. *Sens. Actuat. B: Chem.* **367**, 132163 (2022).
37. Erwin, W. R., Zarick, H. F., Talbert, E. M. & Bardhan, R. Light trapping in mesoporous solar cells with plasmonic nanostructures. *Energy Environ. Sci.* **9**(5), 1577–1601. https://doi.org/10.1039/c5ee03847b (2016).
38. Jimenez-Cisneros, J., Galindo-Lazo, J. P., Mendez-Rojas, M. A., Campos-Delgado, J. R. & Cerro-Lopez, M. Plasmonic spherical nanoparticles coupled withtitania nanotube arrays prepared by anodization as substrates for surface-enhancedraman spectroscopy applications: A review. *Molecules* **26**(24), 145. https://doi.org/10.3390/molecules26247443 (2021).
39. de Aberasturi, D. J., Serrano-Montes, A. B. & Liz-Marzán, L. M. Modern applications of plasmonic nanoparticles: From energy to health. *Adv. Opt. Mater.* **3**(5), 602–617 (2015).
40. Zhao, Y. *et al.* Electrospun TiO2 nanofelt surface-decorated with Ag nanoparticles as sensitive and UV-cleanable substrate for surface enhanced Raman scattering. *ACS Appl. Mater. Interfaces* **6**(8), 5759–5767 (2014).
41. Chaudhary, R. G. & Desimone, M. F. Synthesis, characterization, and applications of green synthesized nanomaterials (part 1). *Curr. Pharm. Biotechnol.* **22**, 722–723 (2021).
42. Mostafa, A. M. & Mwafy, E. A. Environmental nanotechnology. *Monit. Manag.* **14**, 100382 (2020).
43. Rahmah, M. I. Preparation of silver chloride nanoparticles using human urine. *Appl. Nanosci.* **11**(10), 2611–2615 (2021).
44. Ismail, R. A., Mousa, A. M. & Amin, M. H. Effect of laser fluence on the structural, morphological and optical properties of 2H-PbI 2 nanoparticles prepared by laser ablation in ethanol. *J. Inorg. Organometall. Polym. Mater.* **28**, 2365–2374 (2018).
45. Rahmah, M. I., Ahmed, A. M., Rashid, T. M. & Jabbar Qasim, A. Preparation of silver nanoparticles using laser ablation for in vitro treatment of MCF-7 cancer cells with antibacterial activity. Plasmonics. 1–9 (2023).
46. Mousa, A. M., Ismail, R. A. & Amin, M. H. Hybrid p-Au@ PbI2/n-Si heterojunction photodetector prepared by pulsed laser ablation in liquid. *Optik* **183**, 933–941 (2019).
47. Salim, E. T., Agool, I. R. & Muhsien, M. A. Construction of SnO$_2$/SiO$_2$/Si heterojunction and its lineup using I-V and C-V measurements. *Int. J. Mod. Phys. B* **25**(29), 3863–3869. https://doi.org/10.1142/S0217979211102022 (2011).
48. Abdulrazzaq, O. A. & Saleem, E. T. Inexpensive near-IR photodetector. *Turk. J. Phys.* **30**, 35–39 (2006).
49. Omar, M. H., Amin, M. H. & Younis, H. A. Comparison of using nano-ZnO and nano-Al$_2$O$_3$ to improve the properties of prepared polymethyl methacrylate denture base. *Appl. Phys. A* **128**(4), 313 (2022).
50. Chouke, P. B. *et al.* Biosynthesized δ-Bi2O3 Nanoparticles from Crinum viviparum Flower Extract for Photocatalytic Dye Degradation and Molecular Docking. *ACS Omega* **7**, 20983–20993 (2022).
51. Mostafa, A. M., Mwafy, E. A. & Hasanin, M. S. One-pot synthesis of nanostructured CdS, CuS, and SnS by pulsed laser ablation in liquid environment and their antimicrobial activity. *Opt. Laser Technol.* **121**, 105824 (2020).
52. Aadim, K. A. & Jasim, A. S. Silver nanoparticles synthesized by Nd: YAG laser ablation technique: characterization and anti-bacterial activity. *J. Mod. Sci.* **8**, 71–82 (2022).
53. Eisa, W. H. *et al.* Clean production of powdery silver nanoparticles using Zingiber officinale: The structural and catalytic properties. *J. Clean. Prod.* **241**, 118398 (2019).
54. Salim, E. T. Rapid thermal oxidation for silicon nanocrystal based solar cell. *Int. J. Nanoelectron. Mater.* **5**(2), 95–100 (2012).
55. Hattab, F. & Fakhry, M. Optical and structure properties for nano titanium oxide thin film prepared by PLD, in *2012 First National Conference for Engineering Sciences (FNCES 2012)*. https://doi.org/10.1109/NCES.2012.6740474.
56. Muhsien, M. A., Salim, E. T. & Agool, I. R. Preparation and characterization of (Au/n-SnO$_2$ /SiO$_2$/Si/Al) MIS device for opto-electronic application. *Int. J. Opt.* **2013**, 9. https://doi.org/10.1155/2013/756402 (2013).

57. Ismail, R. A., Rasheed, B. G., Salm, E. T. & Al-Hadethy, M. High transmittance-low resistivity cadmium oxide films grown by reactive pulsed laser deposition. *J. Mater. Sci.: Mater. Electron.* **18**(10), 1027–1030. https://doi.org/10.1007/s10854-007-9129-4 (2007).
58. Mostafa, A. M. Preparation and study of nonlinear response of embedding ZnO nanoparticles in PVA thin film by pulsed laser ablation. *J. Mol. Struct.* **1223**, 129007 (2021).
59. Salim, E. T. Optoelectronic properties of Fe_2O_3/Si heterojunction prepared by rapid thermal oxidation method. *Indian J. Phys.* **87**(4), 349–353. https://doi.org/10.1007/s12648-012-0229-5 (2013).
60. Fakhri, M. A., Al-Douri, Y. & Hashim, U. Fabricated optical strip waveguide of nanophotonics lithium niobate. *IEEE Photonics J.* **8**(2), 4500410. https://doi.org/10.1109/JPHOT.2016.2531583 (2016).
61. Muhsien, M. A., Salem, E. T., Agool, I. R. & Hamdan, H. H. Gas sensing of Au/n-SnO_2/p-PSi/c-Si heterojunction devices prepared by rapid thermal oxidation. *Appl. Nanosci.* **4**, 719–732 (2014).
62. Jurn, Y. N. *et al.* Important parameters analysis of the single-walled carbon nanotubes composite materials. *ARPN J. Eng. Appl. Sci.* **11**(8), 5108–5113 (2016).
63. Jeon, J. W. *et al.* The effect of laser pulse widths on laser—Ag nanoparticle interaction: Femto-to nanosecond lasers. *Appl. Sci.* **8**, 112 (2018).
64. Fakhri, M. A. *et al.* Structural properties and surface morphology analysis of nanophotonic $LINBO3$. *ARPN J. Eng. Appl. Sci.* **11**(8), 4974–4978 (2016).
65. Mwafy, E. A., Gaafar, M. S., Mostafa, A. M., Marzouk, S. Y. & Mahmoud, I. S. Novel laser-assisted method for synthesis of SnO_2/MWCNTs nanocomposite for water treatment from Cu (II). *Diam. Relat. Mater.* **113**, 108287 (2021).
66. Fakhri, M. A., Hashim, U., Salim, E. T. & Salim, Z. T. Preparation and charactrization of photonic $LiNbO_3$ generated from mixing of new raw materials using spry pyrolysis method. *J. Mater. Sci.: Mater. Electron.* **27**(12), 13105–13112. https://doi.org/10.1007/s10854-016-5455-8 (2016).
67. Elsayed, K. A. *et al.* Fabrication of ZnO–Ag bimetallic nanoparticles by laser ablation for anticancer activity. *Alex. Eng. J.* **61**(2), 1449–1457 (2022).
68. Al Baroot, A. *et al.* Enhancement of catalytic reduction of 4-nitrophenol using MoO_3 nanobelts incorporated SiO_2 nanocomposite fabricated by nanosecond pulsed laser ablation technique. *Phys. Scr.* **98**(9), 095002 (2023).
69. Manda, A. A. *et al.* Catalytic activity of cellulose acetate butyrate/TiO_2-Au nanocomposite film prepared by laser ablation for 2-nitrophenol reduction. *J. Polym. Environ.* **32**, 1–12 (2023).
70. Al Baroot, A. *et al.* Anticancer activity of Au/CNT nanocomposite fabricated by nanosecond pulsed laser ablation method on colon and cervical cancer. *Micromachines* **14**(7), 1455 (2023).
71. Alheshibri, M. *et al.* Tuning the morphology of Au/ZnO nanocomposite using pulsed laser ablation for anticancer applications. *Arab. J. Sci. Eng.* **49**, 1–12 (2023).
72. Alheshibri, M. *et al.* Synthesis of highly stable Ag/Ta_2O_5 nanocomposite by pulsed laser ablation as an effectual antibacterial agent. *Opt. Laser Technol.* **162**, 109295 (2023).
73. Al Baroot, A. *et al.* Photocatalytic performance of Ag/TiO_2/SiO_2 nanocomposite synthesized by eco-friendly pulsed laser ablation technique. *J. Phys. Chem. Solids* **180**, 111489 (2023).
74. Al Baroot, A. *et al.* Investigating the antibacterial activity of nanostructured tungsten oxide prepared by pulsed laser ablation at different hydrogen peroxide concentrations. *Opt. Mater.* **133**, 112886 (2022).
75. Manda, A. A. *et al.* Synthesis of CuO/α-Fe_2O_3 nanocomposite by Q-switched pulsed laser ablation and its catalytic activity for environmental applications. *Arab. J. Sci. Eng.* **48**(6), 7635–7646 (2023).
76. AlBaroot, A. *et al.* A novel approach for fabrication ZnO/CuO nanocomposite via laser ablation in liquid and its antibacterial activity. *Arab. J. Chem.* **15**(2), 103606 (2022).
77. Elsayed, K. A. *et al.* Anticancer activity of TiO_2/Au nanocomposite prepared by laser ablation technique on breast and cervical cancers. *Opt. Laser Technol.* **149**, 107828 (2022).
78. Tahani, F. *et al.* Physicochemical properties of nanofluids produced from oxidized nanoparticles synthesized in a liquid by pulsed laser ablation. *Lasers Manuf. Mater. Process.* **9**, 1–19 (2022).
79. Al-Otaibi, A. L. *et al.* Pulsed laser ablation-mediated facile fabrication of MoO_3/TiO_2/rGO nanocomposite as a photocatalyst for dye degradation. *Opt. Laser Technol.* **170**, 110156 (2024).
80. Alamro, F. S., Mostafa, A. M., Al-Ola, K. A. A., Ahmed, H. A. & Toghan, A. Synthesis of Ag nanoparticles-decorated CNTs via laser ablation method for the enhancement the photocatalytic removal of naphthalene from water. *Nanomaterials* **11**, 2142 (2021).
81. Fakhri, M. A. *et al.* Enhancement of Lithium Niobate nanophotonic structures via spin-coating technique for optical waveguides application. *Eur. Phys. J. Conf.* **162**(7), 01004. https://doi.org/10.1051/epjconf/201716201004 (2017).
82. Song, S., Wang, X. & Zhang, H. CeO_2-encapsulated noble metal nanocatalysts: enhanced activity and stability for catalytic application. *NPG Asia Mater.* **7**, e179–e179 (2015).
83. Nbelayim, P. *et al.* Preparation and characterization of stable and active Pt@$TiO2$ Core–shell nanoparticles as electrocatalyst for application in PEMFCs. *ACS Appl Energy Mater.* **3**, 3269–3281 (2020).
84. Fatimah, I. *et al.* Magnetic-silica nanocomposites and the functionalized forms for environment and medical applications: A review. *Inorg. Chem. Commun.* **137**, 109213 (2022).
85. Belessiotis, G. V. *et al.* Magnetic metal oxide-based photocatalysts with integrated silver for water treatment. *Materials* **15**, 4629 (2022).
86. Long, Y. *et al.* Construction of trace silver modified core@shell structured Pt-Ni nanoframe@$CeO2$ for semihydrogenation of phenylacetylene. *Nano Res.* **12**, 869–875 (2019).
87. Neyman, K. M. & Kozlov, S. M. Quantifying interactions on interfaces between metal particles and oxide supports in catalytic nanomaterials. *NPG Asia Mater.* **14**, 59 (2022).
88. Ishida, T. *et al.* Importance of size and contact structure of gold nanoparticles for the genesis of unique catalytic processes. *Chem. Rev.* **120**, 464–525 (2020).
89. Rupprechter, G. Operando surface spectroscopy and microscopy during catalytic reactions: From clusters via nanoparticles to meso-scale aggregates. *Small* **17**, 2004289 (2021).
90. Rai, P. Plasmonic noble metal@metal oxide core–shell nanoparticles for dye-sensitized solar cell applications. *Sustain. Energy Fuels* **3**, 63–91 (2019).
91. Liu, X. *et al.* Noble metal–metal oxide nanohybrids with tailored nanostructures for efficient solar energy conversion, photocatalysis and environmental remediation. *Energy Environ. Sci.* **10**, 402–434 (2017).
92. Zhang, Q. *et al.* Core–shell nanostructured catalysts. *Acc. Chem. Res.* **46**, 1816–1824 (2013).
93. Rai, P. *et al.* Noble metal@metal oxide semiconductor core@shell nano-architectures as a new platform for gas sensor applications. *RSC Adv.* **5**, 76229–76248 (2015).
94. Li, G. & Tang, Z. Noble metal nanoparticle@metal oxide core/yolk–shell nanostructures as catalysts: Recent progress and perspective. *Nanoscale* **6**, 3995–4011 (2014).
95. Ismail, R. A., Salim, E. T. & Halbos, H. T. Preparation of Nb_2O_5 nanoflakes by hydrothermal route for photodetection applications: The role of deposition time. *Optik* **245**, 167778 (2021).

96. Alsultany, F. H., Alhasan, S. F. H. & Salim, E. T. Seed layer-assisted chemical bath deposition of Cu_2O nanoparticles on ITO-coated glass substrates with tunable morphology, crystallinity, and optical properties. *J. Inorg. Organomet. Polym.* **31**, 3749–3759. https://doi.org/10.1007/s10904-021-02016-y (2021).

97. Abdul-Hamead, A. A., Othman, F. M. & Fakhri, M. A. Preparation of $MgO–MnO_2$ nanocomposite particles for cholesterol sensors. *J. Mater. Sci. Mater. Electron.* **32**, 15523–15532 (2021).

98. Abood, M. K., Salim, E. T., Saimon, J. A. & Hadi, A. A. Electrical conductivity, mobility and carrier concentration in Nb_2O_5 films: Effect of NH_4OH molarity. *Int. J. Nanoelectron. Mater.* **14**(3), 259–268 (2021).

99. Hassan, M. A., Al-Nedawe, B. M. & Fakhri, M. A. Embedded optical fiber link interferometer sensors for snapshot surface inspection using the synthetic wavelength technique. *Appl. Opt.* **60**(8), 2339–2347 (2021).

100. Mohsin, M. H., Numan, N. H., Salim, E. T. & Fakhri, M. A. Physical properties of sic nanostructure for optoelectronics applications. *J. Renew. Mater.* **9**(9), 1519–1530 (2021).

101. Fakhri, M. A. *et al.* The structure and optical properties of Lithium Niobate grown on quartz for photonics application. *Eur. Phys. J. Conf.* **162**, 01005. https://doi.org/10.1051/epjconf/201716201005 (2017).

102. Lijie, X., Yin, M. & Liu, S. F. Superior sensor performance from Ag@ WO3 core–shell nanostructure. *J. Alloys Compd.* **623**, 127–131 (2015).

103. Fakhri, M. A., Basheer, R. A., Banoosh, A. M. & Azeez, H. N. Rapid thermal oxidation of nano silver film for solar cell fabrication. *Digest J. Nanomater. Biostruct.* **16**(2), 367–375 (2021).

104. Khan, M., Kumar, S., Ahamad, T. & Alhazaa, A. Enhancement of photocatalytic and electrochemical properties of hydrothermally synthesized WO_3 nanoparticles via Ag loading. *J. Alloys Compd.* **743**, 485–493 (2018).

105. Hassen, H. H. *et al.* Fourier transform infrared spectroscopy and photo luminance results for Zno NPs prepared at different preparation condition using LP-PLA technique. *Int. J. Nanoelectron. Mater.* **11**(Special Issue BOND21), 65–72 (2018).

106. Davis, E. A. & Mott, N. F. Conduction in non-crystalline systems V. Conductivity, optical absorption and photoconductivity in amorphous semiconductors. *Philos. Mag.* **22**(179), 0903–0922 (1970).

107. Salim, E. T., Saimon, J. A., Abood, M. K. & Alsultany, F. H. A preliminary study on structural and optical properties of heat treated Nb_2O_5 nanostructure. *Int. J. Nanoelectron. Mater.* **16**(1), 21–32 (2023).

108. Hassan, N. K., Khalid, F. G., Ekshayesh, A. A., Dahham, O. S. & Hussein, M. M. Optical investigations of gold nano rods and gold nano rods doped with ZnO nanoparticles for optoelectronic applications. *J. Opt. (India)* **52**, 2023–2030. https://doi.org/10.1007/s12596-023-01120-1 (2023).

109. Osamah, S., Alwahib, A. A., Fakhri, M. A. & Gopinath, S. C. B. Study of single and symmetrical D-shaped optical fiber sensor based on gold nanorods. *J. Opt. (India)* **52**, 2048–2058. https://doi.org/10.1007/s12596-023-01119-8 (2023).

110. Imam, M. A. & Chopra, N. *Morphological, Structural and Optical Characterization of Bottom-Up Growth of Ag–WO3 Core-Shell Nano-Cube Heterostructures* (2017).

111. Abdul Amir, H. A. A., Fakhri, M. A. & Alwahib, A. A. Review of GaN optical device characteristics, applications, and optical analysis technology. *Mater. Today: Proc.* **42**, 2815–2821 (2021).

112. Xu, L., Yin, M.-L. & Liu, S. F. Agx@WO3 core–shell nanostructure for LSP enhanced chemical sensors. *Sci. Rep.* **4**, 6745 (2014).

113. Shi, W. & Chopra, N. Controlled fabrication of photoactive copper oxide–cobalt oxide nanowire heterostructures for efficient phenol photodegradation. *ACS Appl. Mater. Interfaces* **4**(10), 5590–5607 (2012).

114. Hassan, N. K., Fakhri, M. A., Salim, E. T. & Hassan, M. A. Gold nano particles based optical fibers for a different sensor in a review. *Mater. Today: Proc.* **42**, 2769–2772 (2021).

115. Chopra, N., Shi, W. & Lattner, A. Fabrication and characterization of copper oxide (CuO)–gold (Au)–titania (TiO2) and copper oxide (CuO)–gold (Au)–indium tin oxide (ITO) nanowire heterostructures. *Mater. Character.* **96**, 71–77 (2014).

116. Tumuluri, A., Naidu, K. L. & Raju, K. J. Band gap determination using Tauc's plot for LiNbO3 thin films. *Int. J. ChemTech Res.* **6**(6), 3353–3356 (2014).

117. Alghurabi, M. N. A. K., Mahmood, R. S., Salim, E. T., Alhasan, S. F. H. & Khalid, F. G. Structure, optical, and morphological investigations of nano copper oxide prepared using RPLD at different laser wavelength effects. *Mater. Today: Proc.* **42**, 2497–2501 (2021).

118. Amir, H. A. A. A. *et al.* Synthesis of gallium nitride nanostructure using pulsed laser ablation in liquid for photoelectric detector. *Mater. Sci. Semicond. Process.* **150**, 106911 (2022).

119. Mohammed, D. A., Kadhim, A. & Fakhri, M. A. The enhancement of the corrosion protection of 304 stainless steel using Al_2O_3 films by PLD method. *AIP Conf. Proc.* **2045**(1), 020014. https://doi.org/10.1063/1.5080827 (2018).

120. Salim, E. T., Ismail, R. A. & Halbos, H. T. Deposition geometry effect on structural, morphological and optical properties of Nb_2O_5 nanostructure prepared by hydrothermal technique. *Appl. Phys. A* **126**, 891 (2020).

121. Hassan, M. M., Fakhri, M. A. & Adnan, S. A. Structural electrical and detection properties of copper oxide based on optoelectronic device. *IOP Conf. Ser.: Mater. Sci. Eng.* **454**(1), 012172. https://doi.org/10.1088/1757-899X/454/1/012172 (2018).

122. Bunaciu, A. A., UdriŞTioiu, E. G. & Aboul-Enein, H. Y. X-ray diffraction: Instrumentation and applications. *Crit. Rev. Anal. Chem.* **45**(4), 289–299 (2015).

123. Salim, E. T., Saimon, J. A., Abood, M. K. & Fakhri, M. A. Effect of silicon substrate type on Nb_2O_5/Si device performance: an answer depends on physical analysis. *Opt. Quantum Electron.* **52**(10), 463 (2020).

124. Fakhri, M. A. *et al.* Synthesis and characterization of GaN/quartz nanostructure using pulsed laser ablation in liquid. *Phys. Scr.* **97**(11), 115813. https://doi.org/10.1088/1402-4896/ac9866 (2022).

125. Awayiz, M. T. & Salim, E. T. Photo voltaic properties of Ag_2O/Si heterojunction device: Effect of substrate conductivity. *Mater. Sci. Forum* **1002**, 200–210 (2020).

126. Ali, H. S. & Fakhri, M. A. An overview of Au & photonic crystal fiber of sensors. *Mater. Sci. Forum* **1002**, 282–289 (2020).

127. Mahdi, R. O., Fakhri, M. A. & Salim, E. T. Physical investigations of niobium oxide nanorod imploring laser radiation. *Mater. Sci. Forum* **1002**, 211–220 (2020).

128. Cullity, B. D. *Elements of X-ray diffraction* (Addison-Wesley PUBLISHING, 1956).

129. Fakhri, M. A. *et al.* A gold nanoparticles coated unclad single mode fiber-optic sensor based on localized surface plasmon resonance. *Sci. Rep.* **13**, 5680 (2023).

130. Adam, H., Gopinath, S. C. B., Md Arshad, M. K., Sasidharan, S. & Wu, Y. S. Integration of microfluidic channel on electrochemicalbased nanobiosensors for monoplex and multiplex analyses: an overview. *J. Taiwan Inst. Chem. Eng.* **146**, 104814 (2023).

131. Taleb, S. M., Fakhri, M. A. & Adnanm, S. A. Optical Investigations of nanophotonic LiNbO3 films deposited by pulsed laser deposition method, defect and diffusion. *Forum* **398**, 16–22 (2020).

132. Hassan, M. M., Fakhri, M. A. & Adnan, S. A. Structural and morphological properties of nano photonic silicon structure for photonics applications, defect and diffusion. *Forum* **398**, 29–33 (2020).

133. Adnan, S. A., Tawfiq, Z. H. & Fakhri, M. A. Gold nanoparticles in liquid based on photonic crystal fiber PCF for sensors application, defect and diffusion. *Forum* **398**, 23–28 (2020).

134. Fakhri, M. A. *et al.* The effect of annealing temperature on optical and photolumence proper. *Surf. Rev. Lett.* **26**(10), 1950068. https://doi.org/10.1142/S0218625X19500689 (2019).

135. Salim, E. T., Awayiz, M. T. & Mahdi, R. O. Tea concentration effect on the optical, structural, and surface roughness of Ag_2O thin films. *Digest J. Nanomater. Biostruct.* **14**(4), 1151–1159 (2019).

136. Hassan, M. M., Fakhri, M. A. & Adnan, S. A. 2-D of nano photonic silicon fabrication for sensing application. *Digest J. Nanomater. Biostruct.* **14**(4), 873–878 (2019).
137. Taleb, S. M., Fakhri, M. A. & Adnan, S. A. Physical investigations of nanophotonic LiNbO₃ films for photonic applications. *J. Ovonic Res.* **15**(4), 261–269 (2019).
138. Jiawang, M. et al. Composition of Ag–WO₃ core-shell nanostructures as efficient electrocatalysts for hydrogen evolution reaction. *J. Solid State Chem.* **271**, 246–252 (2019).
139. Ro, I., Resasco, J. & Christopher, P. Approaches for understanding and controlling interfacial effects in oxide-supported metal catalysts. *ACS Catal.* **8**, 7368–7387 (2018).
140. Badr, B. A., Mohammed, Q. Q., Numan, N. H., Fakhri, M. A. & Abdul Wahhab, A. W. Substrate temperature effects on optical properties and constants of ZnO. *Int. J. Nanoelectron. Mater.* **12**(3), 283–290 (2019).
141. Abdulrahman, T. E., Salim, E. T., Mahdi, R. O. & Wahid, M. H. A. Nb2O5 nano and microspheres fabricated by laser ablation. *Adv. Nat. Sci. Nanosci. Nanotechnol.* **13**, 045006. https://doi.org/10.1088/2043-6262/ac99cf (2022).
142. Imam, M. A. & Chopra. N. *Morphological, Structural and Optical Characterization of Bottom-Up Growth of Ag–WO₃ Core-Shell Nano-cube Heterostructures* (2017).
143. Salim, E. T. et al. Effect of light induced heat treatment on the structural and morphological properties of LiNbO3 thin films. *Super Lattices Microstruct.* **128**, 67–75. https://doi.org/10.1016/j.spmi.2019.01.016 (2019).
144. Xu, L., Yin, M.-L. & Liu, S. Agx@WO3 core-shell nanostructure for LSP enhanced chemical sensors. *Sci. Rep.* **4**, 6745 (2015).
145. Ahemad, M. J., Le, T. D., Kim, D.-S. et al. Bimetallic AgAu alloy@ZnO Core–Shell Nanoparticles for Ultra-High Detection Of Ethanol: Potential Impact of Alloy.
146. Abood, M., Salim, E. T. & Saimon, J. A. Optical investigations of Nb₂O₅ at different teamperatures for optoelectronic devices. *J. Ovonic Res.* **15**(2), 109–115 (2019).
147. Salim, E. T. & Halboos, H. T. Synthesis and physical properties of Ag doped niobium pentoxide thin films for Ag-Nb₂O₅/Si heterojunction device. *Mater. Res. Express* **6**(6), 066401. https://doi.org/10.1088/2053-1591/ab07d3 (2019).
148. Badr, B. A., Numan, N. H., Khalid, F. G., Fakhri, M. A. & Abdulwahhab, A. W. Effects of substrate temperatures on optical properties and constants of ZnO prepared by PLD. *J. Ovonic Res.* **15**(2), 127–133 (2019).
149. Fakhri, M. A., Abdulwahhab, A. W., Kadhim, S. M., Alwazni, M. S. & Adnan, S. A. Thermal oxidation effects on physical properties of CuO₂ thin films for optoelectronic application. *Mater. Res. Express* **6**(2), 026429 (2018).
150. Wu, C.-C. Highly flexible touch screen panel fabricated with silver inserted transparent ITO triple-layer structures, I. *RSC Adv.* **8**(22), 11862–11870 (2018).
151. Huang, P.-S., Qin, F. & Lee, J.-K. Role of the interface between Ag and ZnO in the electric conductivity of Ag nanoparticle-embedded ZnO. *ACS Appl. Mater. Interfaces* **12**(4), 4715–4721 (2019).
152. Fakhri, M. A. et al. Efficiency enhancement of optical strip waveguide by the effect of heat treatment. *Optik* **180**, 768–774. https://doi.org/10.1016/j.ijleo.2018.12.006 (2019).
153. Suresh, S., Gautam E., Unni, M., Satyanarayana, A., Nair, S. & Pillai, V.P.M. Ag@ Nb₂O₅ plasmonic blocking layer for higher efficiency dye-sensitized solar cells. *Dalton Trans.* **47**(13), 4685–4700 (2018).
154. Salim, E. T., Shafeeq, S. R., AbdulRazzaq, M. J., Fakhri, M. A. & Gopinath, S. C. B. Photo-activation of Ag chemicals for enhanced Nb₂O₅ optoelectronic device employing plasmonic effects. *Surf. Interfaces* **36**, 102618 (2023).
155. Salim, E. T., Saimon, J.A., Abood, M. K. & Fakhri, M. A. Electrical conductivity inversion for Nb₂O₅ nanostructure thin films at different temperatures. *Mater. Res. Express* **6**(12), 126459. https://doi.org/10.1088/2053-1591/ab771c (2019).
156. Salim, E. T., Hassan, A. I., Mohamed, F. A. & Fakhri, M. A. Photoactivation of Ag ions for improved WO₃-based optoelectronic devices. *J. Opt.* https://doi.org/10.1007/s12596-023-01596-x (2024).
157. Badr, B. A., Numan, N. H., Khalid, F. G., Fakhri, M. A. & Abdulwahhab, A. W. All optical investigations of copper oxide for detection devices. *J. Ovonic Res.* **15**(1), 53–59 (2019).
158. Al Wazny, M. S., Salim, E. T., Bader, B. A. & Fakhry, M. A. Synthesis of Bi₂O₃ films, studying their optical, structural, and surface roughness properties. *IOP Conf. Ser. Mater. Sci. Eng.* **454**(1), 012160. https://doi.org/10.1088/1757-899X/454/1/012160 (2018).
159. Halboos, H. T. & Salim, E. T. Silver doped niobium pentoxide nanostructured thin film, optical structural and morphological properties. *IOP Conf. Ser. Mater. Sci. Eng.* **454**(1), 012174. https://doi.org/10.1088/1757-899X/454/1/012174 (2018).
160. Tawfiq, Z. H., Fakhri, M. A. & Adnan, S. A. Photonic crystal fibres PCF for different sensors in review. *IOP Conf. Ser.: Mater. Sci. Eng.* **454**(1), 012173. https://doi.org/10.1088/1757-899X/454/1/012173 (2018).
161. Cisneros-Contreras, I. R., Muñoz-Rosas, A. L. & Rodríguez-Gómez, A. Resolution improvement in Haacke's figure of merit for transparent conductive films. *Results Phys.* https://doi.org/10.1016/j.rinp.2019.102695 (2019).
162. Amin, M. H. et al. A comprehensive investigation of structural, optical, morphological, and electrical properties of CuO-NPs synthesized by pulsed laser ablation in water: Effect of laser fluence. *J. Mater. Sci.: Mater. Electron.* **35**, 210. https://doi.org/10.1007/s10854-024-11954-5 (2024).
163. Mohammed, D. A., Fakhri, M. A. & Kadhim, A. Reduction the corrosion rate of 304 stainless steel using pulsed laser shock penning method. *IOP Conf. Ser.: Mater. Sci. Eng.* **454**(1), 012162. https://doi.org/10.1088/1757-899X/454/1/012162 (2018).

Acknowledgements

Author contributions

Conceptualization, E.T., J.A., M.S., A.S., R.I., M.A., and M.H.; methodology, E.T., J.A., M.S., A.S., R.I., M.A., and M.H.; validation, E.T., J.A., M.S., A.S., R.I., M.A., and M.H.; formal analysis, E.T., J.A., M.S., A.S., R.I., M.A., and M.H.; investigation, E.T., J.A., M.S., A.S., R.I., M.A., and M.H.; resources, E.T., J.A., M.S., A.S., R.I., M.A., and M.H.; data curation, E.T., J.A., M.S., A.S., R.I., M.A., and M.H.; writing—original draft preparation, M.S., and M.H.; writing—review and editing, E.T., J.A., A.S., R.I., and M.A.,; visualization, E.T., J.A., M.S., A.S., R.I., M.A., and M.H.; supervision, E.T., and J.A.; project administration, E.T., J.A., M.A.; funding acquisition, providing own funds, Each author has reviewed the published version of the manuscript and given their approval.

Competing interests

The authors declare no competing interests.

Additional information

Correspondence and requests for materials should be addressed to E.T.S., M.A.F. or A.S.A.

Reprints and permissions information is available at www.nature.com/reprints.

Publisher's note Springer Nature remains neutral with regard to jurisdictional claims in published maps and institutional affiliations.